AGU PUBLICATIONS

JGR

Journal of Geophysical Research: Planets

RESEARCH ARTICLE
10.1002/2013JE004590

Special Section:
Results from the first 360 Sols of the Mars Science Laboratory Mission: Bradbury Landing through Yellowknife Bay

Key Points:
- Rocks show morphologic diversity but similar chemistry
- Rocknest rocks have high Fe and low Mg that sets them apart
- They may be fine-grained sediments with an iron-rich cement

Supporting Information:
- Readme
- Table S1
- Figure S1
- Figure S2
- Figure S3

Correspondence to:
D. L. Blaney,
diana.l.blaney@jpl.nasa.gov

Citation:
Blaney, D. L., et al. (2014), Chemistry and texture of the rocks at Rocknest, Gale Crater: Evidence for sedimentary origin and diagenetic alteration, *J. Geophys. Res. Planets*, *119*, 2109–2131, doi:10.1002/2013JE004590.

Received 7 DEC 2013
Accepted 6 AUG 2014
Accepted article online 14 AUG 2014
Published online 10 SEP 2014

Chemistry and texture of the rocks at Rocknest, Gale Crater: Evidence for sedimentary origin and diagenetic alteration

D. L. Blaney[1], R. C. Wiens[2], S. Maurice[3], S. M. Clegg[2], R. B. Anderson[4], L. C. Kah[5], S. Le Mouélic[6], A. Ollila[7], N. Bridges[8], R. Tokar[9], G. Berger[3], J. C. Bridges[10], A. Cousin[2], B. Clark[11], M. D. Dyar[12], P. L. King[13], N. Lanza[2], N. Mangold[6], P.-Y. Meslin[3], H. Newsom[7], S. Schröder[3], S. Rowland[14], J. Johnson[8], L. Edgar[15], O. Gasnault[3], O. Forni[3], M. Schmidt[16], W. Goetz[17], K. Stack[18], D. Sumner[19], M. Fisk[20], and M. B. Madsen[21]

[1]Jet Propulsion Laboratory, California Institute of Technology, Pasadena, California, USA, [2]Los Alamos National Laboratory, Los Alamos, New Mexico, USA, [3]UPS-OMP; Institute de Recherche en Astrophysique et Planetologie, Université Paul Sabatier, Toulouse, France, [4]U.S. Geological Survey Astrogeology Science Center, Flagstaff, Arizona, USA, [5]Earth and Planetary Sciences, University of Tennessee, Knoxville, Knoxville, Tennessee, USA, [6]LPG Nantes, CNRS, UMR6112, Université Nantes, Nantes, France, [7]Institute of Meteoritics, University of New Mexico, Albuquerque, New Mexico, USA, [8]Johns Hopkins University Applied Physics Laboratory, Laurel, Maryland, USA, [9]Planetary Science Institute, Tucson, Arizona, USA, [10]Space Research Centre, Department of Physics and Astronomy, University of Leicester, Leicester, UK, [11]Space Science Institute, Boulder, Colorado, USA, [12]Department of Astronomy, Mount Holyoke College, South Hadley, Massachusetts, USA, [13]Research School of Earth Sciences, Australia National University, Canberra, ACT, Australia, [14]SOEST, University of Hawai'i at Mānoa, Honolulu, Hawaii, USA, [15]School of Earth and Space Exploration, Arizona State University, Tempe, Arizona, USA, [16]Department of Earth Sciences, Brock University, St. Catharines, Ontario, Canada, [17]Max-Planck-Institut für Sonnensystemforschung, Katlenburg-Lindau, Germany, [18]California Institute of Technology, Pasadena, California, USA, [19]Department of Geology, University of California, Davis, California, USA, [20]College of Earth, Ocean, and Atmospheric Sciences, Oregon State University, Corvallis, Oregon, USA, [21]Niels Bohr Institute, Astrophysics and Planetary Science, University of Copenhagen, Copenhagen, Denmark

Abstract A suite of eight rocks analyzed by the Curiosity Rover while it was stopped at the Rocknest sand ripple shows the greatest chemical divergence of any potentially sedimentary rocks analyzed in the early part of the mission. Relative to average Martian soil and to the stratigraphically lower units encountered as part of the Yellowknife Bay formation, these rocks are significantly depleted in MgO, with a mean of 1.3 wt %, and high in Fe, averaging over 20 wt % FeO_T, with values between 15 and 26 wt % FeO_T. The variable iron and low magnesium and rock texture make it unlikely that these are igneous rocks. Rock surface textures range from rough to smooth, can be pitted or grooved, and show various degrees of wind erosion. Some rocks display poorly defined layering while others seem to show possible fractures. Narrow vertical voids are present in Rocknest 3, one of the rocks showing the strongest layering. Rocks in the vicinity of Rocknest may have undergone some diagenesis similar to other rocks in the Yellowknife Bay Formation as indicated by the presence of soluble calcium phases. The most reasonable scenario is that fine-grained sediments, potentially a mixture of feldspar-rich rocks from Bradbury Rise and normal Martian soil, were lithified together by an iron-rich cement.

1. Introduction

The Gale Crater landing site was selected for the "Curiosity" rover [*Grotzinger et al*., 2012] because of the diversity of geologic features observed from orbit [*Malin and Edgett*, 2000; *Anderson and Bell*, 2010; *Thompson et al*., 2011; *Wray*, 2013] including aerially extensive sedimentary deposits associated with a well-defined geomorphic fan [*Sumner et al*., 2013; *Williams et al*., 2013], a thick package of layered deposits within Aeolis Mons [*Malin and Edgett*, 2000; *Milliken et al*., 2010], and a series of low-albedo, active dunes [*Hobbs et al*., 2010; *Silvestro et al*., 2013], which together suggest a complex sedimentary history within Gale Crater.

The Curiosity rover spent nearly 40 sols (Martian solar days = 24.6 h) exploring a region called Rocknest (Figure 1). The Rocknest site consists of a local topographic high that marks the northern edge of a broad, aeolian sand shadow [*Blake et al*., 2013; *Minitti et al.*, 2013]. These aeolian materials were chosen as the first solid sample to be measured by Curiosity [*Anderson et al*., 2012; *Edgett et al*., 2012; *Minitti et al.*, 2013, *Gellert et al*., 2013; *Blake et al*., 2012; *Bish et al*., 2013; *Mahaffy et al*., 2012; *Leshin et al*., 2013].

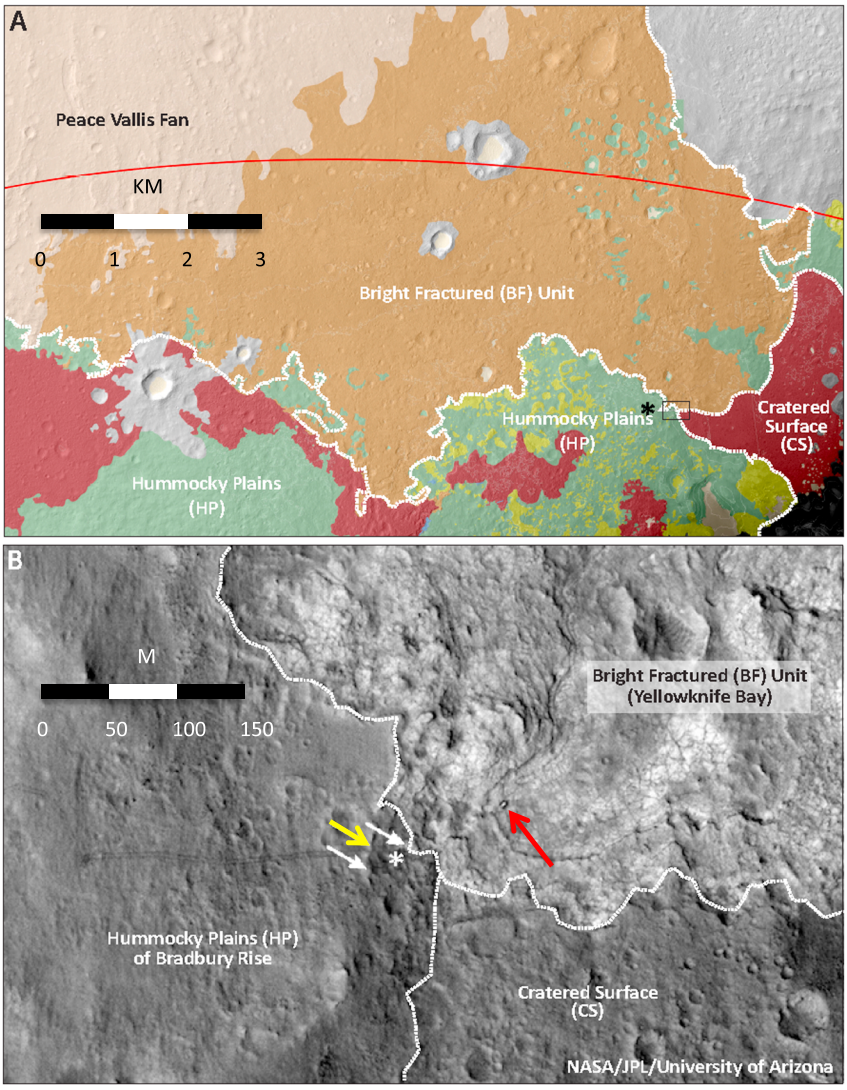

Figure 1. (a) Orbital view of the landing site with different surface units represented by different colors. The outline of the final landing ellipse is marked by a red curve. The landing site, within the Hummocky Plains, is marked by an asterisk. The inset marked by the rectangle to the right of the landing site is shown in Figure 1b. (b) The image shows the rover tracks across Bradbury Rise with the Rocknest location marked by an asterisk. The rover can be seen as a white dot to the right, in Yellowknife Bay, and is pointed at by a red arrow. (White arrows indicate locations where the rover stopped to collect geochemical data; Yellow arrow is location of Bathurst Inlet and Cowels Lake targets).

In addition to aeolian materials, exposed rocks were present for Curiosity to investigate. During the stay at Rocknest, ChemCam had the opportunity to analyze a variety of rocks and soils [*Meslin et al.*, 2013; *Cousin et al.*, 2013; *Goetz et al.*, 2013], and the Alpha Particle X-ray Spectrometer (APXS) analyzed two rocks [*Schmidt et al.*, 2014]. Here we report on ChemCam textural and geochemical analyses of rocks exposed at Rocknest, in order to explore both the chemical variability within a given rock and variability between rocks of similar and different textures.

2. Observations and Methods

ChemCam utilizes laser-induced breakdown spectroscopy (LIBS) to provide elemental composition at distances up to 7 m from the rover and accompanies these analyses with high-resolution imaging using the Remote Microscopic Imager (RMI) [*Maurice et al.*, 2012a, 2012b; *Wiens et al.*, 2012, 2013a]. Analysis spot size ranges from 350 μm to 550 μm depending on range [*Maurice et al.*, 2012a, 2012b]. A given analysis spot is

Table 1. ChemCam LIBS Observations of Rocknest Rocks

Target	Distance (m)	Sol	Sequence	Observation
Pearson	3.6	61	ccam01060	3 × 3
		68	ccam02067	3 × 3
		79	ccam02079	3 × 3
Peg	3.8	71	ccam03071	3 × 3
Rocknest 3	3.7	57	ccam01057	1 × 5 diagonal
		82	ccam01082	1 × 10 vertical
		84	ccam01083	1 × 10 vertical
		88	ccam01088	5 × 5 (only 15 on target)
Rocknest 6	2.6	71	ccam01071	3 × 3
		88	ccam04087	3 × 3
		88	ccam05087	3 × 3
Snare	2.9	70	ccam01069	5 × 1 horizontal
Walsh	4.4	79	ccam03079	3 × 3
Zephyr	2.7	71	ccam02071	3 × 3 (three hit target)

fired upon repeatedly by the laser (generally from 30 to 50 laser shots), and the emission spectrum from each laser shot is recorded. Typically, multiple locations are interrogated within a given observation. In the Rocknest region, observations were made using five- and 10-point line scans or square grids of 3 × 3 or 5 × 5 analysis locations. Passive spectra (collected with no laser plasma present) were also obtained before each active LIBS spectrum. These passive reflectance spectra allow accurate subtraction of the non-LIBS light and can also be used to investigate the reflectance of the individual analysis locations [*Johnson et al.*, 2013].

Images were collected with the ChemCam Remote Microscopic Imager (RMI) at the beginning and end of ChemCam observations, centered respectively on the first and last LIBS points in a line scan or grid. Additional images were added if the areal extent covered by LIBS was sufficiently large to require additional coverage. RMI images permit localization of the ChemCam laser spots and provide high-resolution images for the textural interpretation of the target [*Le Mouélic et al.*, 2013]. Together, ChemCam LIBS and RMI can be used for high-resolution investigations and enable the detection/discrimination of chemical layering and other small-scale features that are not detectable with instruments such as APXS, which integrate analyses over a larger area. The repeated laser pulses of a typical ChemCam observation can remove surface dust and reveal near-surface changes in chemistry. A summary of the sequences and observations made with ChemCam at Rocknest is provided in Table 1.

In addition to ChemCam observations, Mastcam returned extensive imaging of the entire Rocknest region. Two of the rocks in this area (Et Then and Rocknest 3) were investigated by the arm-mounted instruments: the Alpha-Particle X-ray Spectrometer (APXS) [*Schmidt et al.*, 2014] and the Mars Hand Lens Imager. The proximity of Et Then to the rover, however, prohibited ChemCam analysis of this sample. The CheMin instrument analyzed none of the rocks at Rocknest; therefore, the mineralogy of these samples is not known.

Calibration targets on the back of the rover were used to check the accuracy and precision of the ChemCam sampling. These targets consist of three synthetic glasses and one natural glass [*Fabre et al.*, 2011] representing different igneous compositions and four sintered ceramic targets representing potential sedimentary targets [*Vaniman et al.*, 2012]. The ceramics, which were produced with varying amounts of sulfates, display heterogeneity at the scale of the LIBS beam, so only the glass samples were used to characterize the precision of measurements on Mars.

3. Geologic Setting of Rocknest Rocks

The Curiosity rover landed within an area informally named Bradbury Rise. Bradbury Rise consists of a generally smooth textured unit referred to as the Hummocky Plains (HP) [*Grotzinger et al.*, 2013] that lies near the toe of the Peace Vallis fan, a large alluvial fan extending from a channel that cuts the northern rim of the crater. The stratigraphic relationship between the Hummocky Plains and the Peace Vallis fan, however, is not yet established [*Grotzinger et al.*, 2013]. The surface of Bradbury rise HP unit consists of angular float, rounded pebbles and gravels, and occasional outcrops of pebble conglomerate [cf. *Wiens et al.*, 2013a; *Yingst et al.*, 2013]. Conglomerates represent the first in-place bedrock encountered by the Curiosity rover and

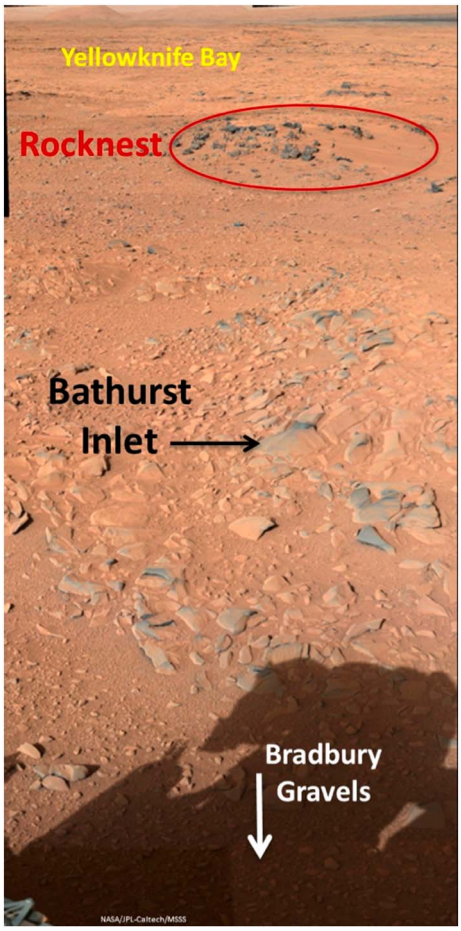

Figure 2. View ahead of the rover from sol 52 location showing the physical relationship between the Bathurst ridge (foreground), Rocknest (middle), and Yellowknife Bay (background). Rocknest is roughly 24 m away. (MCAM image numbers/0052ML024 0000000E1_DXXX, 0052ML0240001000E1_DXXX, 0052ML0240002000E1_DXXX, 0052ML0240003 000E1_DXXX, 0052ML0240007000E1_DXXX 0052ML 0240008000E1_DXXX, 0052ML0240009000E1_DXXX).

suggest that channelized flow and bed load transport of sedimentary materials may have been widespread across Bradbury rise [*Williams et al*., 2013].

The Rocknest outcrop lies near the intersection of the Hummocky Plains of Bradbury Rise, light-toned layered strata—the Bright Fractured (BF) unit of Yellowknife Bay and a regional exposure of a low-albedo, Cratered Surface (CS) unit (Figure 1) that may represent an impact gardened resistant horizon that caps layered strata of Yellowknife Bay. At first glance, both the textural complexity of the Rocknest site and its position at the juncture of the Hummocky Plains, Cratered Surface, and Bright Fractured units suggest that exposed rock may represent material from more than one of these geomorphic units.

Along the traverse into the Rocknest region, the Curiosity rover descended through a resistant ridge of fine-grained, layered rocks that included the Bathurst Inlet outcrop and Cowles Lake target. The ridge containing these two rocks (Figure 1b) appears to be in stratigraphic continuity with light-toned, layered strata of Yellowknife Bay and has been mapped as the uppermost part of the Glenelg member of the Yellowknife Bay formation developed within Yellowknife Bay [*Grotzinger et al*., 2013]. The physical relationship between this ridge, the Rocknest outcrop, and other strata of the Yellowknife Bay formation can be seen in Figure 2 which shows the perspective approaching Rocknest after the sol 52 drive from roughly 24 m away. Some similarity of texture between Bathurst member strata and fine-grained, laminated rocks of the northwestern edge of the Rocknest outcropping (see details below) suggests a potential genetic linkage between Rocknest rocks and layered rocks of Yellowknife Bay [*McLennan et al*., 2013].

Images taken with the Navigation Cameras provide a broader local context for Rocknest (Figure 3). Rocks of

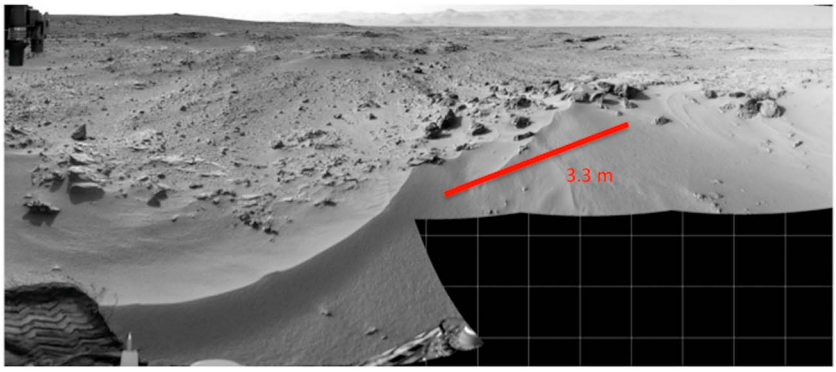

Figure 3. Sol 57 Navigation Camera end of drive mosaic (sequence ID: Sol 57, navcam00446) showing Rocknest relationship with surrounding outcrop. Distance from Rocknest 6 to Walsh is ~3.3 m. Outcrops can be traced to the Rocknest sand dune suggesting that these rocks are locally derived or outcrop.

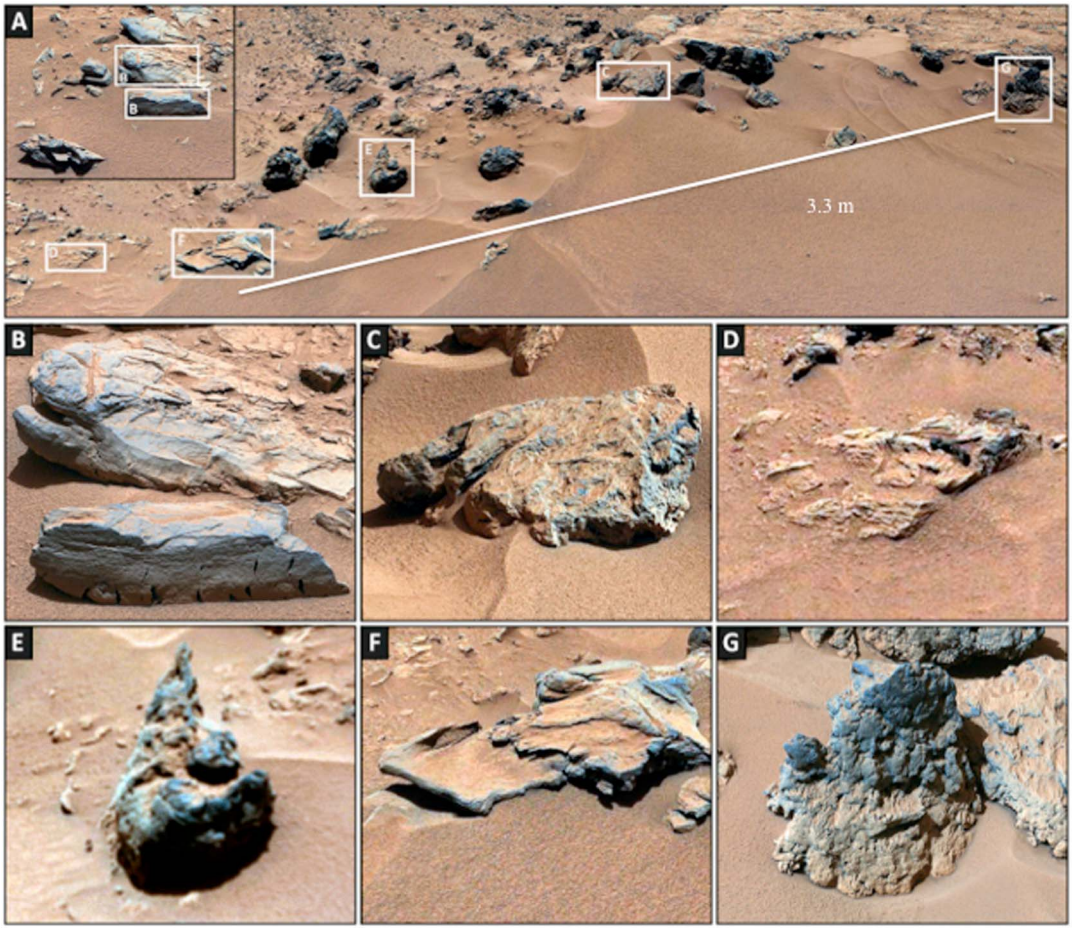

Figure 4. (a) Mastcam images of the rocks observed by ChemCam at Rocknest. Individual panels show (b) Rocknest 3 (foreground) and Peg (behind), (c) Pearson, (d) Zephyr, (e) Snare, (f) Rocknest 6, and (g) Walsh. (Rocknest 3 image: Mastcam 0059ML0269000000E1, Rocknest Mosaic Mastcam Image # 0066ML029600000I1_DXXX, 0066ML0296001000E1_DXXX, 0066ML029600100I1_DXXX, 0066ML0296002000E1_DXXX, 0066ML029600200I1_DXXX, 0066ML0296003000E3_DXXX, 0066ML029600300I1_DXXX, 0066ML0296004000E1_DXXX).

similar albedo and texture can be traced to the Rocknest area from exposed outcrop, suggesting that these rocks represent either bedrock or locally derived rocks.

Descending ~ 3 m from the Rocknest outcrop to lower stratigraphic levels, the rover encountered the Gillespie Lake and Sheepbed members of the Yellowknife Bay formation [*Grotzinger et al*., 2013]. The lowest stratigraphic member, the Sheepbed member, is characterized as mudstone whose chemical composition broadly mimics current Martian soils but almost completely lacks sulfur [*McLennan et al*., 2013]. The mineral composition of Sheepbed consists of pyroxene, plagioclase, calcium sulfate, iron oxide or hydroxide, iron sulfide, and amorphous minerals and includes approximately 20% phyllosilicate minerals. The mudstone contains much the same mineral composition as the Rocknest soil but with notably less olivine, suggesting that the olivine may have been largely converted to clay minerals plus magnetite within the Sheepbed depositional environment [*Vaniman et al*., 2013; *McLennan et al*., 2013].

The Gillespie member, which directly overlies the Sheepbed member, appears to be a coarser-grained sandstone of similar composition to the Sheepbed mudstone [*Grotzinger et al*., 2013]. Finally, the Glenelg member consists of a heterogeneous assemblage of interstratified rocks ranging from fine-grained sandstone to pebbly sandstone to conglomeratic units [*Grotzinger et al*., 2013; *Edgar et al*., 2013]. The Glenelg member includes (from bottom to top) Point Lake, Shaler, Rocknest, and Bathurst outcrops although the rocks of these outcrops may be partially interstratified and their exact sequence remains uncertain. The Shaler outcrop consists of discrete fine- to coarse-grained sandstone beds separated by recessive,

Table 2. Rocknest Rocks Texture Classification

Target	Texture	Erosion Style	RMI
Pearson	Massive		Fine grained. Voids several millimeters in size, slightly elongated. Higher density of lineaments (fractures?) producing enhanced vertical topography.
Peg	Laminated		Fine grained, laminated, ventifacted, some lineaments (fractures?) producing some topography.
Rocknest 3	Laminated		Fine grained, laminated, top ventifacted. Side has small voids several millimeters in size, slightly elongated, large vertical voids, possible layering.
Rocknest 6	Laminated	Platy	Fine grained, laminated. Clear grooves from abrasion with remnant eroded voids, oriented lineaments/fabric.
Snare	Massive		Fine grained. Voids several millimeters in size, slightly elongated. Higher density of lineaments (fractures?) producing enhanced vertical topography.
Walsh	Massive		Fine grained. Voids several millimeters in size, slightly elongated. Higher density of lineaments (fractures?) producing enhanced vertical topography.
Zephyr	Laminated	Resistant	Fine grained, laminated. Resistant piece rising from rock. Some voids visible with oriented lineaments/fabric.

presumably finer grained (possibly siltstone to mudstone) intervals. These strata are distinctly cross-bedded, suggesting dominantly fluvial transport, with intermittent aeolian activity [*Grotzinger et al*., 2013]. Conglomeratic to pebbly sandstone of the Point Lake outcrop displays similarities to some of the more rough textured Rocknest rocks. The fine-grained rocks of the Bathurst member are both spatially and stratigraphically close to the Rocknest outcrop and may have close genetic affinities.

4. Texture of Rocknest Rocks

For this paper, we focus on the rocks known as Pearson, Peg, Rocknest 3 (which was also an APXS analysis target), Rocknest 6, Snare, Walsh, and Zephyr. The rock locations and names are shown in Figure 4. Rocknest 3 is shown as an inset due to its proximity to the rover precluded it from being incorporated into the Mastcam mosaic of Rocknest. Due to the Rocknest sand shadow, aeolian material combined with the ubiquitous dust coverage of the regional surface, and the heavily dissected nature of the outcrop obscures contact relationships between individual rocks.

All the rocks at Rocknest are relatively low albedo, and the rocks (or the portions of rocks near the dune form contact) have a color similar to that of the soil. Observed vertical rock faces typically have the lowest albedo while the tops of some of the rocks again have coloration similar to the surrounding soil likely due to the accumulation of dust/soil on horizontal surfaces. In passive ChemCam spectra, these rocks show evidence of a nanophase iron oxide signature with no crystalline features (e.g., hematite) [*Johnson et al*., 2013]. Based on their macroscopic properties, these rocks can be classified into two categories: laminated and massive. The laminated rocks can be further categorized by their erosion style. High-level descriptions and classifications are given in Table 2.

4.1. Laminated Rocks

Laminated rocks include Rocknest 3, Rocknest 6, Peg, and Zephyr (Figure 4). Rocknest 3 was described and illustrated in *Grotzinger et al*. [2013] and interpreted as a fine-grained, finely laminated sedimentary rock with early diagenetic desiccation cracks (shown enlarged in Figure 5). Distinct grains are not resolvable in Mastcam images. However, small-scale variation in surface roughness observed in RMI images (Figures 6–8)

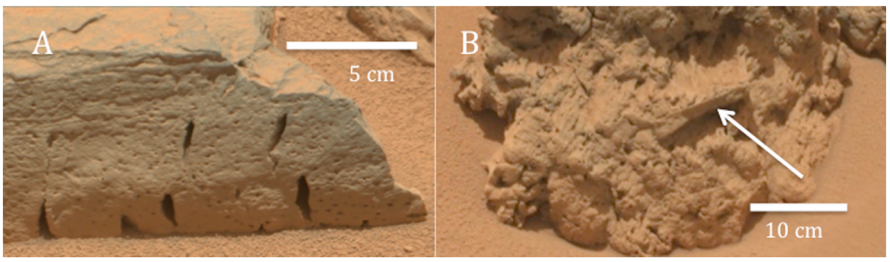

Figure 5. Enlarged Mastcam images of (a) Rocknest 3 (MCAM Image # 0059MR0270002000E1) showing tapered cracks, laminations, and pitting and of (b) Walsh (MCAM Image # 0066ML0296012000E1) showing texture. Arrow in enlargement of Walsh point to an intact/nondeformed block embedded in the rock.

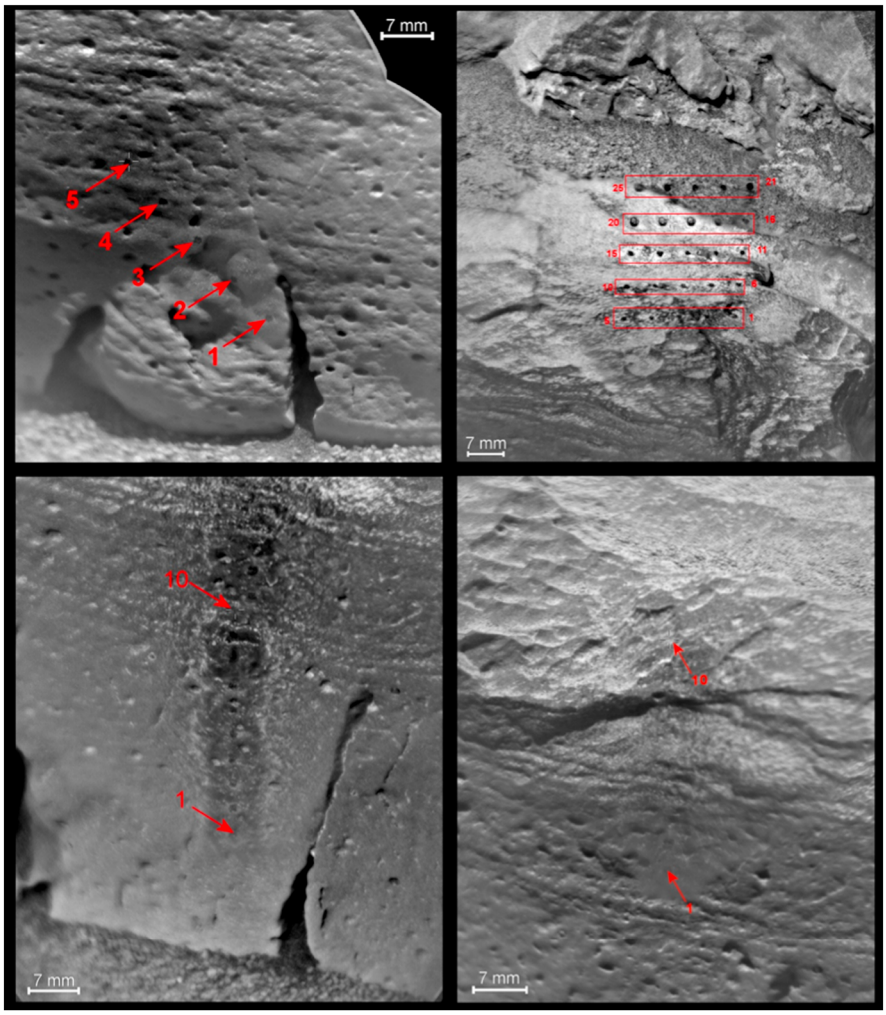

Figure 6. Post LIBS RMI images of Rocknest 3 with laser shots numbered (top left: ccam01057, top right: ccam01088, lower left: ccam01082, and lower right: ccam01083).

indicates a relatively homogeneous, fine-grained matrix. Polishing by wind abrasion suggests that these samples are fairly well cemented and likely contain little of their initial intragranular porosity. Each of these rocks occurs as discrete platy to tabular blocks that show evidence for planar lamination evidenced by a combination of subtle differences in the resistance of the rock to aeolian abrasion and planar fracturing. The presence of lamination is consistent with small changes in grain size, porosity, or cementation. Rocknest 3 and Peg show distinct, well-defined lamination, which is clearly observed on dust-free faces of the tabular blocks in cross section. By contrast, the low profiles of Rocknest 6 and Zephyr inhibit observation of discrete laminations, although their platy morphology suggests the potential for bedding-parallel zones of weakness.

Surface textures vary from smooth (Rocknest 3) to highly fluted (Rocknest 6), to fractured (Peg, Zephyr). The presence of macroscale and microscale fluting (cf. Figure 4, five RMI Rocknest 3 and 6), as well as surficial polishing (Figures 4–7) suggests that these rocks experienced substantial aeolian abrasion. Only Zephyr, however, shows substantial macroscale fluting, which suggests that the fluting may be the result of material properties rather than the amount of erosion/abrasion. By contrast to the smooth and fluted surface textures of Rocknest 3 and 6, rocks Peg and Zephyr show substantial fracturing of their surface. Surface fractures, such as in Peg, appear penetrative, although the surface expression of the fractures appears artificially widened—potentially from wind abrasion. These fractures could be another manifestation of sediment desiccation. Fractures are commonly dust filled/dust covered although fracture fill material cannot be ruled out. This is especially true at Peg (Figure 7).

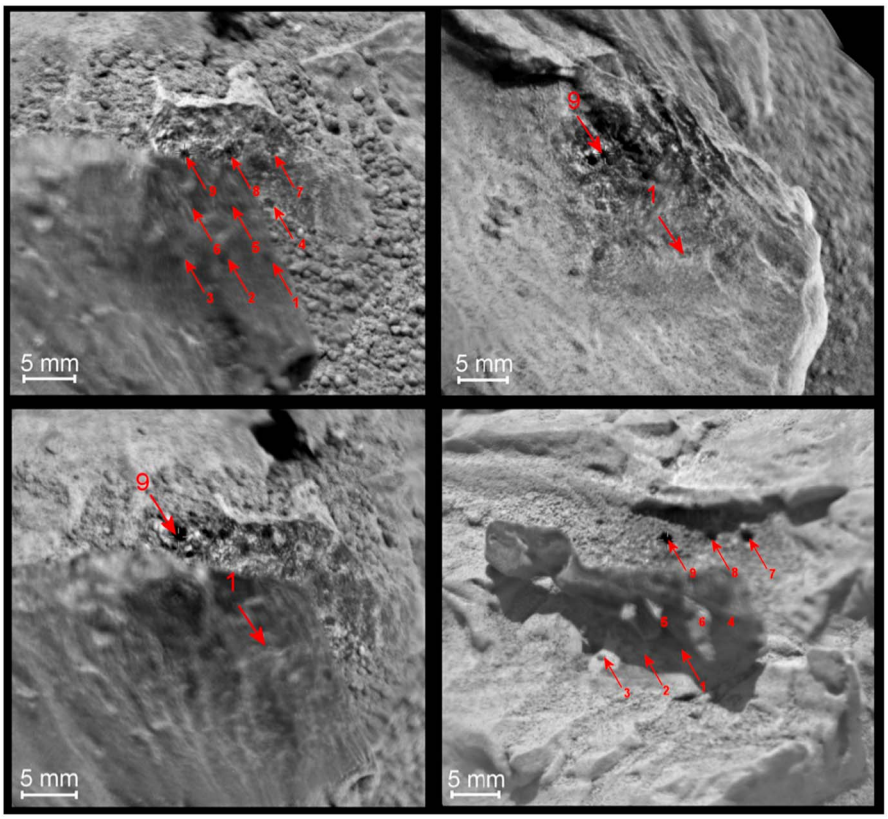

Figure 7. Post LIBS RMI images of Rocknest 6 (top left: ccam01071, top right: ccam04087, and lower left: ccam05087) and Zephyr (lower right: ccam02071).

The most striking textural features of the laminated rocks are a series of striking, tapered cracks that are best expressed on the vertical surface of Rocknest 3 (Figures 4–6). Tapered cracks in Rocknest 3 (cf. Figures 4–6) appear as deep pits that occur in two distinct horizons, are oriented nearly perpendicular to lamination, and pinch out in both upward and, where visible, downward directions. These cracks are similar to desiccation cracks observed in some terrestrial sedimentary rocks [*Grotzinger et al.*, 2013]. Tapered cracks appear, in several instances, however, to extend upward or downward into thin fractures, suggesting that the tapering may alternatively result from the preferential expansion of pervasive fractures within horizons more susceptible to subsequent aeolian abrasion.

In contrast to tapered cracks, surficial pitting appears to be a ubiquitous feature of Rocknest 3 (Figure 6) and may occur as well in Snare (Figure 8) and possibly more irregularly in Pearson (Figure 9). Within Rocknest 3, pits occur as circular to ovoid, shallow pits. These features are substantially larger than observable grain sizes within the rock. Although pits appear uniformly distributed across the observed vertical rock faces, larger and more ovoid pits appear aligned with laminations. On the upper surface of Rocknest 3, smaller pits show a subtle asymmetry with the semimajor axes aligned with the flutes on rock surface. These observations are consistent with aeolian abrasion enlarging preexisting pits. These pits could be preserved void spaces in the rock, possibly of early diagenetic origin from either dissolved minerals or gas features similar to fenestrae in terrestrial rocks.

Another post lithification feature is observed within Zephyr. Zephyr is a heavily eroded rock, largely covered by air fall dust. A single, irregular feature on the top of Zephyr protrudes above the rock (Figure 7), suggesting that the rock is substantially more resistant to aeolian abrasion. The feature is roughly linear, about 20 mm in length, and it is nearly entirely eroded from the primary rock matrix.

4.2. Massive Rocks

Massive rocks include Pearson, Snare, and Walsh (Figures 4, 5, 8, and 9). The morphology of rough-textured rocks varies from broadly tabular, but lacking indication of internal lamination (Pearson), to highly irregular

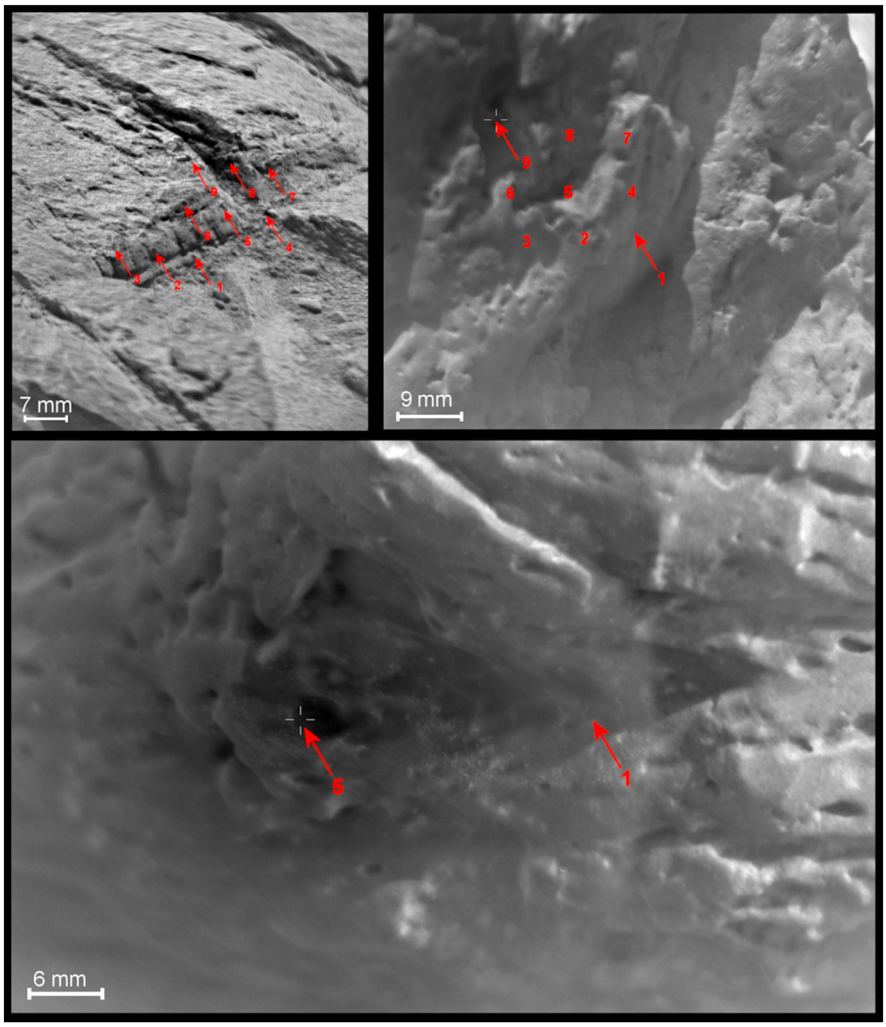

Figure 8. Post LIBS RMI images of Peg (top left: ccam03071), Walsh (top right: ccam03079), and Snare (bottom: ccam01069).

with numerous protrusions and indentations (Walsh, Snare). Snare has an elongate teardrop shape that is reminiscent of a volcanic bomb or impact ballistic block, but such textures are commonly observed in ventifacts also. At higher resolutions afforded by the ChemCam RMI, however, Snare and Walsh, which have irregular shapes and protrusions, appear to consist of a relatively uniform, fine-grained matrix with substantial pitting and an absence of distinct lamination.

Pitting within rough-textured rocks is also more varied from that observed within the laminated rocks. In addition to the small round to ovoid pits similar to those observed in Rocknest 3, rough-textured rocks also preserve a variety of irregular, to oblong, to linear pitting features (Figures 8 and 9). Pearson, in particular, preserves a series of randomly oriented, angular pitting features reminiscent of either the presence of a secondary mineral phase or removal of angular clasts. All pitting shows evidence for wind-induced modification. The variety of shapes preserved by pitting suggests the potential for more than one mechanism of pit formation, including, but not limited to, modification of primary void space within the rock by wind (e.g., enlargement of a pit) or the removal and modification of a primary or secondary mineral (or rock) phase.

A tabular clast is embedded in Walsh (see Figure 5b, enlargement). The clast could have been incorporated during formation as intact fragment in the unlithified rock. A cold massive emplacement may have generated the rough-textured material such as a mud flow or impact ejecta in soft materials. The lack of pebbles point toward transport of the material either locally or via low energy. On Earth, similar textures can result from destabilization of sediments or other soft material during burial.

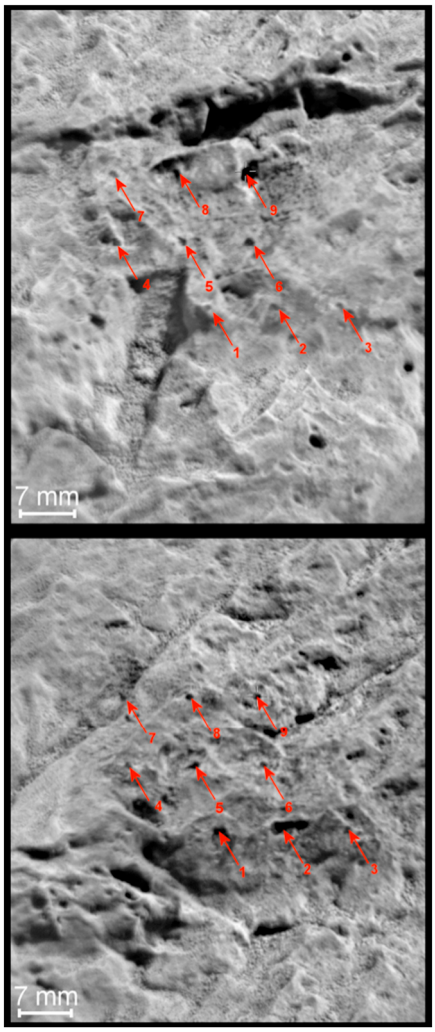

Figure 9. Post LIBS RMI images of Pearson (top: ccam01060 and bottom: ccam0182).

4.3. ChemCam Laser Pits

Additional information on the rocks' hardness and physical properties can be determined by looking for the presence and size of pits in the rocks generated by ChemCam's laser (Figures 6–9). The depth of the holes depends on the hardness of the rock. At Rocknest, ablation pit diameters are on average ~0.8 mm but range in size from 0.6 to 1.4 mm. The relatively large pit diameter suggests weak cementation and that they are relatively soft. Laboratory measurement suggests profiling rates on the order of 0.5–1 μm per shot suggesting penetration depths of 15–30 μm for soft rocks [e.g., *Wiens et al*., 2012]. The softness of the rocks also argues against a dense igneous rock. These laboratory results also have been confirmed at Gale Crater where igneous rocks (such as Bathurst and Jake_M) do not show laser ablation pits but the Rocknest and Yellowknife Bay rocks do.

4.4. Textural and Geomorphic Evidence for Sedimentary Origin

Several lines of textural and geomorphic evidence point toward these rocks being sedimentary in origin, with at least one potential diagenetic event. Ready abrasion of rock surfaces suggests that rock strength is not compatible with that expected from extrusive or intrusive igneous rocks. Finely laminated rocks are consistent with small changes in grain size, porosity, or cementation in sedimentary rocks.

Absence of distinct lamination, in combination with the irregular morphology of the massive rocks, suggests a fundamentally different depositional mode from that of laminated rocks, wherein massive textures likely result from single, substantially larger depositional event(s). Irregular rock morphology and an abundance of irregular protrusions and indentations may represent original rock fabric or modification during or after emplacement in their current outcrop position.

Possible diagenetic features in these rocks include the distinctive pitting, tapered cracks in the laminated rocks, and the fractures in the massive rocks. For the pits, there are two possible formation mechanisms: (1) a primary void space within the rock or (2) the surficial removal of either a primary or secondary mineral phase. The former of these mechanisms seems unlikely; in the absence of discrete gas bubbles in the substrate—which have been proposed as a formation mechanism for hollow nodules in the Sheepbed member of the Yellowknife Bay formation [*Grotzinger et al*., 2013; *Stack et al*., 2014]—it is unlikely that interparticle void space would form discrete voids larger than the observed grain sizes. The presence of a single, homogeneously distributed primary mineral phase is also unlikely. The difference in size between matrix grains and surficial pits suggests that a primary mineral phase would have to be of substantially different composition and mineral density to have allowed transport of such larger grains with matrix components. A more realistic scenario might involve the diagenetic formation, and subsequent removal, of a secondary mineral phase within the original fine-grained matrix. Tapered cracks and fractures within Rocknest rocks provide additional complexity. Fracture formation may represent sediment contraction as it dewaters, similar to the preferred mechanism for the Yellowknife bay fractures [*Grotzinger et al*., 2013]. Alternatively, cracks may represent gas expansion within the substrate [*Grotzinger et al*., 2013] or aeolian modification of fracture that formed post lithification. Other potentially diagenetic features are the Zephyr resistant phase and perhaps the tabular fragment located in Walsh. The Zephyr feature bears some resemblance to the "Snake" feature seen near John Klein, which was interpreted to be an intrusive sandstone dike [*Grotzinger et al*., 2013].

5. ChemCam Major Element Chemistry

5.1. Method

ChemCam utilizes LIBS to provide remote elemental compositions using multiple laser shots, typically distributed over a number of different observation points on a target [*Wiens et al*., 2013a]. Typically, the first five shots at any given location are not included in rock analysis due to the potential contamination by Martian air fall dust and other fine-grained materials. In general, compositions reach a stable composition within the first five laser shots [*Blaney et al*., 2013; *Lanza et al*., 2013]. However, transitions between grains of different compositions have been observed as a function of shot number (a proxy for depth), generally in coarser-grained rocks such as encountered on Bradbury Rise. To check for this the spectra are inspected on a shot by shot basis before being averaged.

The ChemCam LIBS probe integrates 350–550 μm spots with multiple laser shots to determine the geochemical composition of the sample. ChemCam investigations typically probe several locations from which geochemical heterogeneity along the surface of the rock. Compositional heterogeneity can be thoroughly investigated with ChemCam on four different spatial scales. The average composition of a region is determined by probing multiple rocks/outcrops. Variations within a region were analyzed by looking at the chemical variations between targets at Rocknest. Next we looked at chemical variations within a target. Finally, we investigated composition with respect to depth. A total of 119 individual observations on seven different rock targets were analyzed. Most observations were collected with 30 individual LIBS shots.

ChemCam LIBS data processing is done by first subtracting the ambient spectra from the LIBS spectra, denoising the resulting spectra, removing the continuum, and correcting for the instrument response. For major element abundances, the spectra are compared to a spectral library covering 65–67 certified standards depending on the oxide [*Wiens et al*., 2013a]. These spectra were obtained using the ChemCam instrument under Mars-like conditions prior to launch. Spectra and their chemical analyses were individually inspected to assess their accuracy, and outliers for specific elements were removed. The comparison takes the form of a partial least squares (PLS) algorithm using principal components [e.g., *Wiens et al*., 2013; *Clegg et al*., 2009; *Tucker*, 2010; *Anderson et al*., 2012]. The specific algorithm used in this analysis is known as PLS1, and for a given element, the algorithm regresses the target spectra against only the abundances of that particular element.

Determination of sulfur abundances utilized a unique analysis. LIBS spectra at Mars atmospheric pressure display only weak sulfur emission lines [*Sallé et al*., 2004; *Dyar et al*., 2010]. Although the full width at half maximum of the peaks are generally only approximately three channels wide [*Wiens et al*., 2012], an improvement is gained by summing the emission under each peak into a single channel and using PLS on the resulting spectra after having processed the training set in the same way.

5.2. Rocknest Chemistry

Major element abundances expressed as oxide wt % for all 119 Rocknest rock observations are provided in Table S1 in the supporting information. The top line of Table S1 in the supporting information and the top line in Table 4 show the number of components in the model and the root-mean-square error of prediction (RMSEP). RMSEP is produced by using a leave-one-out cross-validation routine. This method steps through the training set leaving the spectra from one standard out, then generating a model based on the remaining standards and predicting the composition of the standard left out. By repeating this process for each geostandard, the result is a conservative estimate of the accuracy of the model when predicting the composition of true unknown targets, assuming a similar range of compositions under similar conditions. There are some overall differences between observations made in a Mars-like environment prior to launch and the Mars observations themselves. These variations are tracked by using onboard calibration targets [*Fabre et al*., 2011; *Vaniman et al*., 2012]. Calibration target reproducibility can be used to estimate measurement precision as discussed below. In the case of the Rocknest suite, the overall compositions vary much less than the range of the training set. Actual accuracies can be better than the cross-validation RMSEP over a narrow range near the compositional center of the training set, so the RMSEP values may be overestimated for the Rocknest targets. However, the abundances of several elements in the Rocknest suite, namely Fe and K, are well above the mean of the training set. While they are still within the range covered by the training set, they might be subject to greater error than the bulk of the elements that fall near the mean

Table 3. Standard Deviation (1σ) on the Precisions Obtained on Synthetic Glass Norite and Shergottite Rover Calibration Targets for "*n*" Number of Analyses[b]

	n	SiO_2	TiO_2	$Al2O_3$	FeOT	MgO	CaO	Na_2O	K_2O
Norite[a] composition (wt %)		47.9	0.70	14.7	15.9	9.62	12.8	1.53	0.06
Sol 352 (1σ)	9	0.34	0.05	0.12	0.24	0.12	0.32	0.11	-----
Sol 357 (1σ)	9	0.68	0.04	0.21	0.27	0.13	0.50	0.12	-----
Shergottite[a] composition (wt %)		48.4	0.43	10.8	17.6	6.39	14.3	1.57	0.11
Sol 271 (1σ)	7	0.60	0.03	0.18	0.26	0.14	0.37	0.10	0.04
Sol 352 (1σ)	9	0.62	0.04	0.14	0.23	0.15	0.30	0.09	0.04
Sol 357 (1σ)	9	0.37	0.02	0.07	0.12	0.07	0.35	0.11	0.04
Mean (1σ)	5	0.43	0.05	0.13	0.27	0.09	0.30	0.11	0.04
All above Shergottite obs. (1σ)	25	1.53	0.14	0.57	1.83	0.49	0.42	0.49	0.14

[a]Norite and Shergottite compositions are from *Wiens et al.* [2013a].
[b]Exact compositions are given for reference.

of the training set. Comparisons with APXS measurements made at Rocknest indicate that ChemCam abundance accuracies are within the stated RMSEPs. These will be discussed later in section 5.4.

5.3. Relative Precision ChemCam Measurements

Calibration targets on the rover were used to check the precision of the PLS method. For this study of Rocknest rocks, a good understanding of the precision is essential so that compositional differences between locations within a given rock or between different rocks can be understood. For this purpose, three 3×3 rasters of 30 shots each were performed on the Shergottite glass target and two 3×3 rasters were done on the Norite glass target [*Fabre et al.*, 2011] on Mars. In addition, many other individual observations have been made over the first year on the calibration targets. The data were processed using PLS, and the standard deviations of the compositions are given in Table 3. The observations on sols 271 and 352 were done with a manual focus, which is faster than the autofocus normally used on Mars surface targets and which was used on the calibration targets on sol 357. The results are essentially indistinguishable. On sol 271 two of the nine observations missed the target because of a command error so they are not included in the assessment. The results for K_2O for norite are omitted, given the low value of its concentration.

The standard deviations of the nine-point rasters on norite and Shergottite in Table 3 are between 0.34 and 0.68 wt % for SiO_2, and they are generally much smaller for all of the other major elements, showing excellent reproducibility within a given raster on a homogeneous target. The second line from the bottom of Table 3 gives the means of the standard deviations from each raster computed in the rows above. This gives the precision relevant for comparing observation points within rasters, such as for estimating the heterogeneity within a given rock such as Snare, Peg, Zephyr, or Walsh. The bottom line of Table 3 gives the standard deviation obtained over all 25 observations of the Shergottite synthetic glass. The results on these lines show a significantly larger variability between different rasters and observations than within a raster. This is particularly true for SiO_2 and FeO_T that show standard deviations of 1.5 and 1.8 wt %, respectively. We assume that the larger standard deviation between different rasters compared to the statistics within a given raster is due to slight differences in instrumental parameters such as the internal temperature of the laser and potential differences in focusing between the rasters, both of which can change the on-target energy density and therefore the resulting plasma properties. Overall, the relative precision between different rasters needs to be taken into account when comparing elemental abundances between different rocks at Rocknest. Analysis of prelaunch calibration data from ChemCam indicates that the precision of the method does not vary significantly between the short distance of the rover calibration targets (1.6 m) and the Rocknest targets (~3–4 m) [*Wiens et al.*, 2013a].

5.4. Comparison Between APXS and ChemCam

Table 4 summarizes the averaged geochemical data for the rocks and soils at Rocknest. The data from Table S1 in the supporting information were used to generate the average and standard deviations for each individual Rocknest rock and for all the Rocknest rocks. Additionally, 110 individual soil and small-grain elemental measurements at Rocknest were averaged to investigate the influence of local soils in the ChemCam Rocknest rock data. Average values are provided in Table 4. Detailed discussion on the variability

Table 4. Rocknest Average ChemCam Compositions and APXS Rocknest Compositions [from *Schmidt et al.*, 2014][a]

	SiO2		TiO2		Al2O3		FeOT		MgO		CaO		Na2O		K2O		Total Oxide (no S)		SO3	
# Components	8		10		4		7		8		8		10		4				9	
RMSEP	7.1		0.6		3.7		4.0		3.0		3.0		0.7		0.9				4.9	
Target	Ave.	SD	Ave.	SD	Ave.	SD	Ave.	SD	Ave.	SD	Ave.	SD	Ave.	SD	Ave.	SD	Ave.	SD	Ave.	SD
Pearson	51.6	3.5	1.2	0.2	6.5	0.8	22.5	1.7	1.3	0.7	5.5	2.4	1.6	0.5	0.9	0.3	92.3	3.9	9.4	2.7
Peg	52.6	4.5	1.3	0.2	9.1	0.7	16.7	1.5	2.0	0.9	4.8	1.0	2.3	0.3	1.3	0.4	91.8	6.3	3.7	0.9
Rocknest 3	51.0	3.9	1.3	0.3	7.5	1.3	19.9	1.6	1.2	1.2	4.9	1.7	1.9	0.4	0.8	0.3	90.0	6.2	6.6	2.2
Rocknest 6	48.2	4.0	1.1	0.3	6.7	0.9	20.1	1.4	1.0	0.9	4.7	1.2	1.9	0.4	0.6	0.4	85.3	5.6	6.9	1.5
Snare	53.4	0.7	1.3	0.2	6.7	0.7	22.6	0.5	0.6	0.1	4.4	0.6	1.4	0.2	1.1	0.1	92.9	0.9	6.9	1.2
Walsh	51.8	2.6	1.4	0.4	7.2	0.9	23.4	1.4	1.8	1.0	5.3	1.2	1.8	0.4	1.1	0.3	94.1	3.3	9.7	1.4
Zephyr	51.3	2.0	2.1	0.2	9.4	0.5	18.9	1.0	3.2	0.4	5.3	0.3	1.9	0.5	1.5	0.4	95.2	1.8	3.6	0.2
Rocknest 3 (Top)	46.9	2.8	0.9	0.1	6.3	0.8	19.8	1.0	1.2	0.9	4.3	0.7	1.9	0.5	0.4	0.4	83.0	4.3	7.1	1.7
All rocks	50.8	3.9	1.2	0.3	7.2	1.3	20.6	2.3	1.3	1.0	5.0	1.7	1.8	0.4	0.9	0.4	90.1	5.9	7.2	2.6
All soils	42.6	6.4	1.0	0.2	7.5	1.6	15.5	2.7	5.7	1.6	7.2	1.6	1.7	0.6	1.1	0.4	82.0	8.9	3.7	2.5
Portage	41.7	4.3	1.2	0.2	8.4	1.4	14.4	1.7	5.5	1.2	6.8	2.0	1.8	0.5	0.4	0.2	79.9	7.9	5.4	2.2
APXS results[b]	wt %	2σ	wt %	2σ	wt %	2σ	wt %	2σ	wt %	2σ	wt %	2σ	wt %	2σ	wt %	2σ	wt %		wt %	2σ
Portage	42.9	0.47	1.2	0.03	9.4	0.14	19.2	0.12	8.7	0.14	7.3	0.07	2.7	0.10	0.5	0.01	91.9	-	5.5	0.01
Et_Then	45.1	0.50	0.7	0.05	8.4	0.19	26.3	0.17	4.2	0.15	4.3	0.10	4.0	0.18	1.6	0.05	94.6	-	4.1	0.05
Rocknest 3	46.0	0.77	1.0	0.04	10.5	0.13	18.4	0.13	5.3	0.53	6.1	0.09	4.2	0.45	1.9	0.05	93.2	-	4.1	0.05

[a]SD = standard deviation.
[b]APXS values are from *Schmidt et al.* [2014].

of the soils can be found in *Cousin et al.* [2013] and *Goetz et al.* [2013] Finally, APXS results from Rocknest rocks [*Schmidt et al.,* 2014] are included for comparison.

Absolute elemental abundances from APXS and ChemCam are not directly comparable due to the way that the data sets are normalized. APXS normalizes all its elemental oxides to 100% of the elements detected and also frequently removes potential Martian dust effects by normalizing to a sulfur free basis [e.g., *Schmidt et al.*, 2014]. ChemCam estimates do not require that the total oxides add up to 100% and leaves room for major element not quantified such as water-bearing phases. Finally, sample heterogeneity and spatial sampling could also play a role in the cross comparison because the spot sizes of ChemCam and APXS are very different.

However, cross comparisons between the instruments can provide added insight into geochemical trends and independent confirmation of interpretation APXS analyzed two different Rocknest rocks, Rocknest 3, and Et_Then; both were single analyses without brushing [*Schmidt et al.*, 2014] so dust cover influences their measurements. The APXS-derived compositions and 2σ statistical errors are given in Table 4.

The ChemCam observations of Rocknest 3 cover the side facing the rover and one 15-point observation on the top. This observation was actually a 25-point observation in which a number of the last points missed the target, leaving 15 to be included in this analysis (ChemCam Sequence: cam01088). The observation was near and potentially overlapping where the APXS observation was made. The average of this 15-point observation is given in Table 4, Rocknest 3 (Top), and is the best observation for cross comparison between ChemCam and APXS Rocknest 3 results.

When compared, Rocknest 3 Top ChemCam and APXS observations of Rocknest 3 have relatively good agreement. For SiO_2, the mean of these 15 points is 46.9 wt %, a fair amount lower than the overall ChemCam average for Rocknest 3 of 50.8 wt % and $<$ 1 wt % different from the reported APXS observation. The mean TiO_2 there is actually slightly lower than APXS. The ChemCam aluminum on Rocknest 3 Top is lower, at 6.3 versus 10.5 wt % Al_2O_3, although the uncertainties associated with both instruments overlap. Magnesium is significantly lower, at a mean of 1.2 wt % compared to 5.3 wt %, determined by APXS, but it is highly very variable among ChemCam's 15 points ranging from 0 to 3 wt %. RMSEP for MgO with ChemCam is 3.0 wt %. There is some difference in CaO, with 4.0 for ChemCam and 6.1 for APXS, but these are within uncertainty of the element.

The two techniques differ markedly in the alkali elements, where ChemCam appears low on the top of Rocknest 3 (1.9 wt % and 0.44 wt % for Na_2O and K_2O compared to 4.2 and 1.9 wt % for APXS), just as it does in the means for all of the Rocknest observations. It is possible that this represents a bias in either the APXS or the ChemCam data set [*McLennan et al.*, 2013].

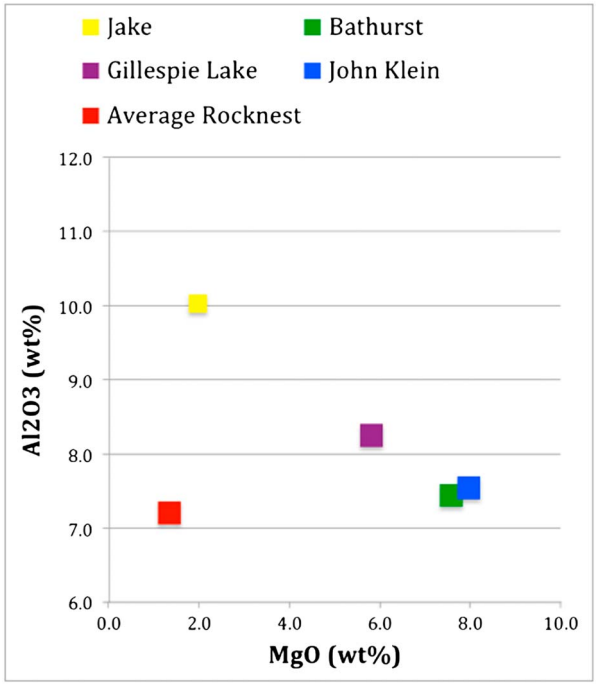

Figure 10. ChemCam average rock MgO and Al_2O_3 for representative rocks seen in Gale Crater.

In addition to differences in measurement technique, surface dust on the target may also cause differences between the results. The APXS observations were unbrushed measurements and that could explain part of the difference in the MgO and SiO_2 abundances between the ChemCam and APXS because the direction of the discrepancy is toward that of the local soil. However, surface dust could play no role in the differences between the alkali abundances because the amounts of alkali elements in the soil at Gale are lower than the Rocknest rocks. Soil contamination would act to lower the alkali abundance in APXS measurements, not increase it.

In an absolute sense ChemCam major results compare well with most APXS elements with the exception of ChemCam results having lower MgO, Na_2O, and K_2O than APXS. These systematic differences are under investigation by the ChemCam team and are currently thought to be the result of limitation in samples in our library currently used for the PLS 1 analysis. A larger sample library is under development [*Clegg et al.*, 2014], but results from this work have not been fully validated and are not available for this analysis.

Iron is a significant exception to the homogeneity of the APXS analyses between Rocknest 3 and Et_Then. The FeO_T observed in Et_Then is 43% higher than that of Rocknest 3 [*Schmidt et al.*, 2014]. The two instruments agree quite well on Rocknest 3 Top, where APXS reports 18.4 wt % and ChemCam reports 19.9 wt % on the rock overall (Table 4) and 19.8 wt % on only the top. The overall range of the ChemCam analyses goes from 14.4 to 25.9 wt % in its point-averaged observations, with the bulk of the observations near 20–22 wt %. Spectra representing individual laser shots within a given observation range slightly higher, to 26.5 wt % within the analysis of location 4 of Walsh (Table S1 in the supporting information). The variability of iron will play a significant role in our discussion of these rocks.

5.5. General Composition Trends

While there is no agreement between the APXS MgO and ChemCam MgO results, both data sets show a depletion in MgO compared to other rocks seen at Gale (Figures 10 and 11) and that the rocks at Rocknest cannot be produced from linearly mixing together other rocks observed at Gale. This is exemplified by the MgO versus Al_2O_3 relationships showing linear trends for most materials at Gale with Rocknest falling well off the line in Figures 10 and 11.

The Rocknest rocks are low in both sodium and potassium, nearly the same as the local soils also calculated using the same PLS1 analysis (Table 4) [*Blake et al.*, 2013]. Within the ChemCam LIBS data set, sodium and potassium are similar to the average soil in the area (Table 4). Iron and silica are significantly higher and magnesium in the rocks significantly lower, making it unlikely that the soils are locally derived in keeping with the *Meslin et al.* [2013] analysis. This is not an unexpected result given that the soils are located in an aeolian dune form which has been mobile in the past.

Rocknest rocks and those of Point Lake, Shaler, and Bathurst differ texturally and compositionally when examined in detail. Overall, both the Shaler and Point Lake outcrops displayed much greater composition and heterogeneity at the scale of the ChemCam beam, showing inclusion of feldspar compositions among a matrix of Sheepbed-like compositions [e.g., *Wiens et al.*, 2013b].

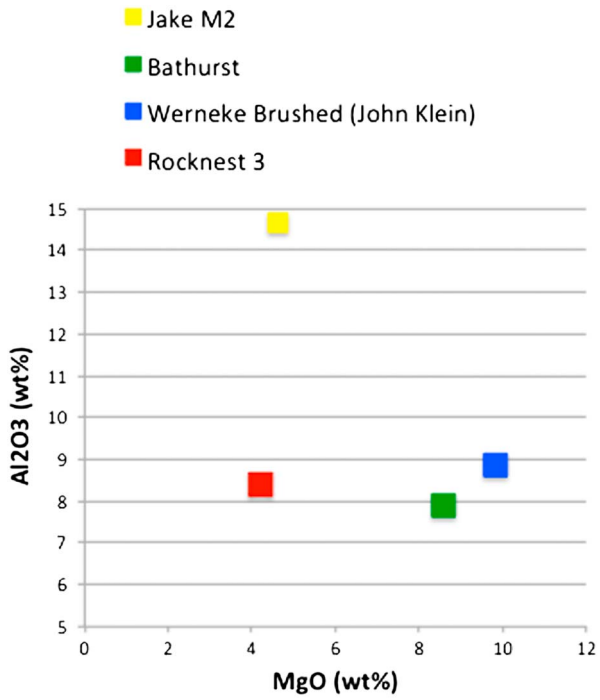

Figure 11. APXS average rock MgO versus Al_2O_3 for representative rocks seen in Gale. Jake_M and Bathurst inlet are from *Schmidt et al.* [2014], and Werneke Brushed is from *McLennan et al.* [2013].

Bathurst, while fine grained like the Rocknest rocks, does not have any of the distinctive ovoid features. Chemically, Bathurst is distinct from the Rocknest Rocks. Bathurst has much lower iron and higher magnesium abundances than the Rocknest rocks [*Schmidt et al.*, 2014; *Sautter et al.*, 2014] that will be discussed further in section 6.

Additionally, these rocks diverge compositionally from the feldspar-rich rocks and pebbles seen earlier and described in *Wiens et al.* [2013a] and *Meslin et al.* [2013]. ChemCam observed more than 60 individual locations during the traverse across Bradbury Rise, and one sample, Jake Matijevic (hereafter "Jake_M"), was sampled by APXS [*Stolper et al.*, 2013]. The Jake_M rock was found to be very similar to alkali-rich rocks typically found in ocean island basalts and was classified as a mugearite. Their feldspar-rich nature requires either relatively high pressure or water-rich magmas or both [*Stolper et al.*, 2013], suggesting significantly more diversity among Martian magmas than was previously thought.

In summary, Rocknest rocks thus far appear unique in composition relative to other rock types being reported by Curiosity. Additionally, the two key features that make the Rocknest rocks unique compared to the rocks at Yellowknife Bay and Bradbury Rise (lower MgO and variable iron with abundances $>$ 25 wt %) are seen clearly in both the APXS and ChemCam data sets.

5.6. Variability Between Rocknest Rocks

For the rest of the paper, we will focus on variability within the ChemCam data set and not the absolute values of the compositions. The fine-grained nature of the rocks as shown in Figures 6–9 imply that each ChemCam observation is measuring a variety of grains smaller than the LIBS spot size. Depending on rock homogeneity, chemical variability will thus be an indicator of the mixture of material sampled at the scale of the LIBS spot. Assuming a sedimentary model for the rocks, each LIBS location included different mixtures of cements and small grains. Because of the large number of locations measured we can determine which elements vary together and look for geochemical trends that are the result of different fractions of cement and grains in a spot. Thus, ChemCam location homogeneity is a proxy for internal chemical variability of the rock at a grain level as the grain size is $<<$ the LIBS spot size. Homogeneous rocks would show little variability. Rocks not as well mixed could show substantially more variability as different fractions of grains are sampled by LIBS measurements. This chemical variability can be examined at both the individual rock spatial scale and across the entire data set. These types of analysis rely on the precision of the LIBS data set, not the absolute accuracy of the PLS results (see Table 4).

To better explain the variability between the rocks at Rocknest, the individual rocks' averages were normalized to the average of all the rocks (Figure 12). Average rock values are very similar for SiO_2. For example, taking the mean of all rocks (Table 4) with an error envelope defined by the bottom row of Table 4, mean values of most of the rocks fall within this range of 49.3–52.3 wt %, with only Snare (53.4), Peg (52.6), and Rocknest 6 (48.2) falling just outside of this range. Calcium also defines a relatively tight range, from 4.4 to 5.5 wt %. We will see later that this range would be even tighter, essentially within the uncertainty defined by Table 4, were it not for approximately three high calcium observations (and approximately three intermediated observations) discussed in section 5.5.

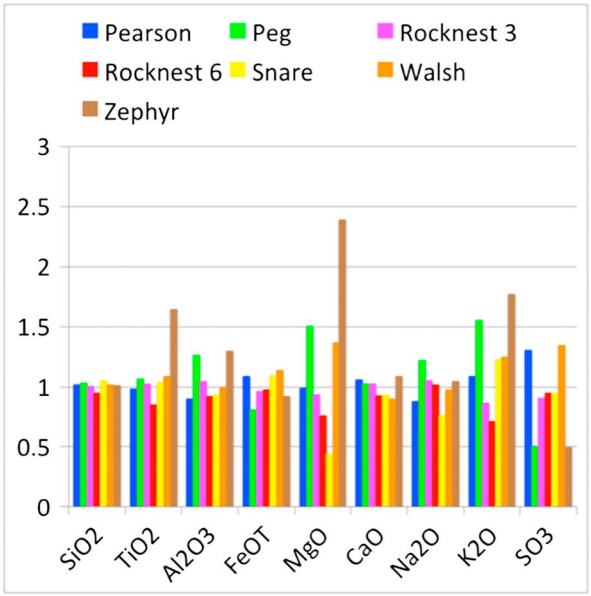

Figure 12. Major element oxide compositions normalized to the average composition of all Rocknest rocks.

The elements showing the largest variation are Mg, K, Ti, and Al. Compared to the average of Rocknest, magnesium is elevated in Zephyr (2.4X higher) Peg (1.5X higher), and to some degree in Walsh (1.3X higher). Zephyr and Peg also have elevated potassium (1.7X higher for Zephyr and 1.5X higher for Peg). Zephyr shows a 1.6X enrichment in Ti. For Zephyr, all three points (Table S1 in the supporting information) are elevated in Mg relative to the Rocknest average, but for Peg and Walsh, there is significant variability between points. Peg Mg ranges from 1 to 4 wt % while Walsh covers the 0.6 to 2.7 wt % range. A general comparison of all of the individual analyses (see the supporting information) indicates that the variability within each rock is essentially as large as between rocks outside of the exceptions noted above. Peg, Walsh, and Zephyr are single-observation measurements so these variations are well outside the ~0.15 standard deviations expected from the caltarget analysis in Table 4.

Variability within each rock for most cases exceeds the calibration target analysis standard deviations in Table 4, implying that the rocks have as much internal compositional variation as there is variation between rocks. Rocks Peg, Snare, Walsh, and Zephyr are represented by single rasters, while Pearson, Rocknest 3, and Rocknest 6 were shot on multiple sols (Table 1). Looking at the Peg, Snare, Walsh, and Zephyr data represented by a single raster, the rocks all exceed the variability of the calibration target for most elements (Table 4) except for Na and K, which appear to have insignificant variations within each rock. A few other rocks show essentially no detectable internal variations for some elements, such as MgO within Snare. Looking in detail at the values in Table S1 in the supporting information (and Figure S1), the chemical variability within the rocks is as great as between the rocks and composition ranges of the most variable elements overlap.

Zephyr is the clearest example where a textural feature corresponds to a chemical signature in the rocks at Rocknest. MgO, K_2O, and TiO_2 differ from the average composition (Figure 12). The three ChemCam points on Zephyr were located on the erosion resistant protrusion. Thus, it is likely that the chemical differences in Mg, Ti, and K are chemical signature of the stronger material.

The differences between the laminate and massive Rocknest rock textures imply either a different depositional environment, modification during emplacement, or diagenetic history. However, except for Zephyr, there are no compositional trends that can be correlated with texture. The overall similarity in composition between the rocks suggests that the process was generally similar chemically. Textural differences are likely caused by either small-scale variations inside individual rocks such as porosity or amount of cement.

5.7. Correlations Between Elements

Figures 12–14 show compositional trends between various elements by looking at all of the individual observation points. Measurements with each rock are color coded, and the average Rocknest soil composition is plotted to help identify measurements that may have been contaminated by Martian soil trapped in rough portions of the rock. In general, these plots show no major soil-rock mixing trends influencing the elemental trends. For instance, measurements that have low iron, similar to soil, have MgO much lower than the soil.

Assuming that each spot is a mixture of cements and grains, we can investigate which elements move in parallel and thus might be carried in the same mineral phase in the rocks. The fine-grained nature of the rock allows for each measurement to sample multiple grains and cements. If we assume that the composition of

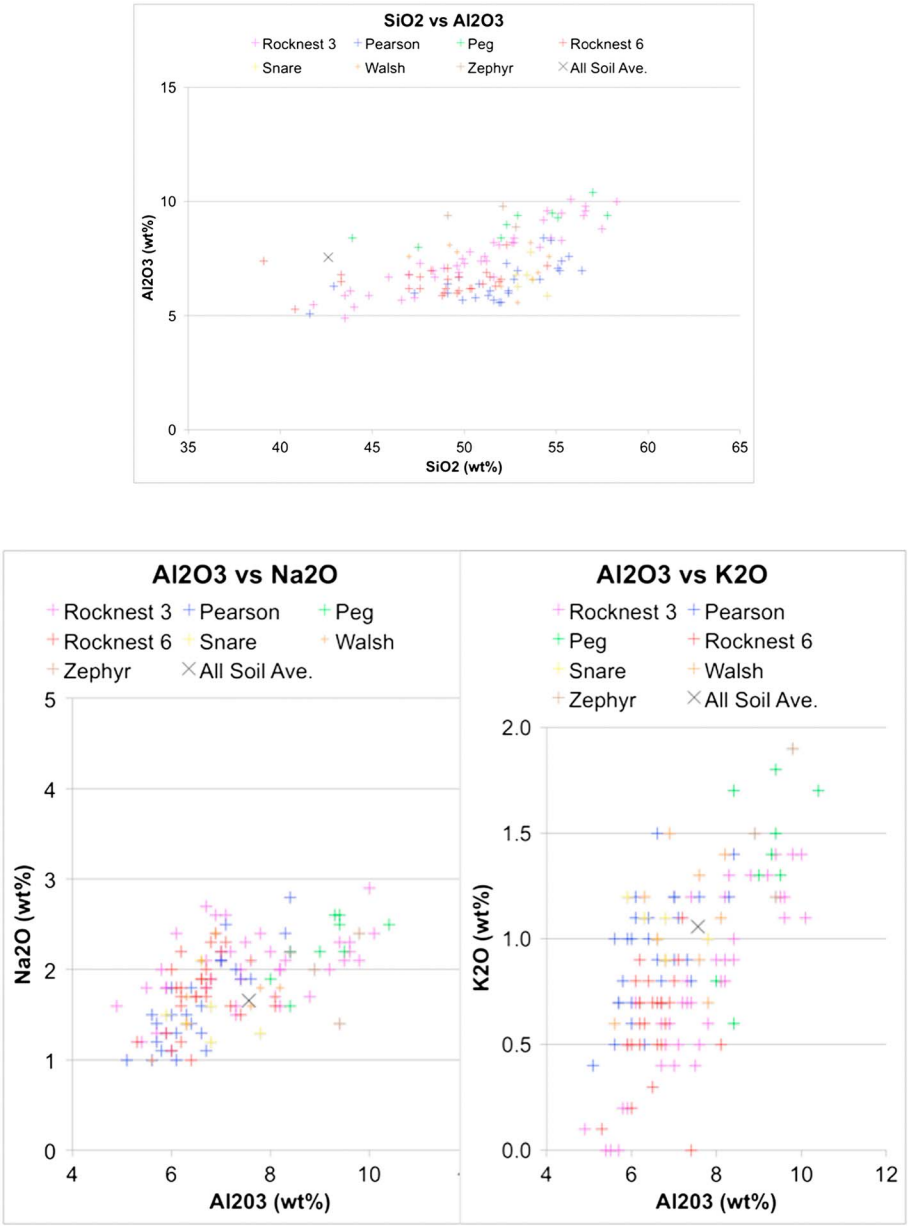

Figure 13. Elemental compositions highlighting trends with SiO_2, Al_2O_3, K_2O, and Na_2O for all of the ChemCam rock observations and for the mean ChemCam soil composition at Rocknest designated by a cross.

the cement and the grains are the same in each observation, chemical variations between measurements are due to sampling different abundances of compositional end-members. As shown in Figure 13, the measurements on Rocknest 3 span the range of compositions for the rest of the rocks for SiO_2 and Al_2O_3 and come close to the full range of sodium and potassium. There are weak positive correlations between the abundances of these elements, with correlation coefficients of 0.33 (SiO_2 versus Al_2O_3), 0.34 (Al_2O_3 versus Na_2O), and 0.43 (Al_2O_3 versus K_2O). These trends indicate that feldspar-rich grains that have been observed in the conglomerates and other rocks on Hummocky Plains unit [*Wiens et al.*, 2013a] are present. However, the low overall abundances of sodium, potassium, and aluminum indicate that feldspar-rich minerals are not the sole silica component of the rock. Grains with a more basaltic (soil-like) composition are also required.

Trends with iron are potentially important given the variability of this element. Four key trends are apparent in Figure 14. Comparison with SiO_2 shows the highest abundances of FeO_T correlating with moderate SiO_2 abundances. This is consistent with the APXS observation of Et_Then, with its high FeO_T abundance, having a

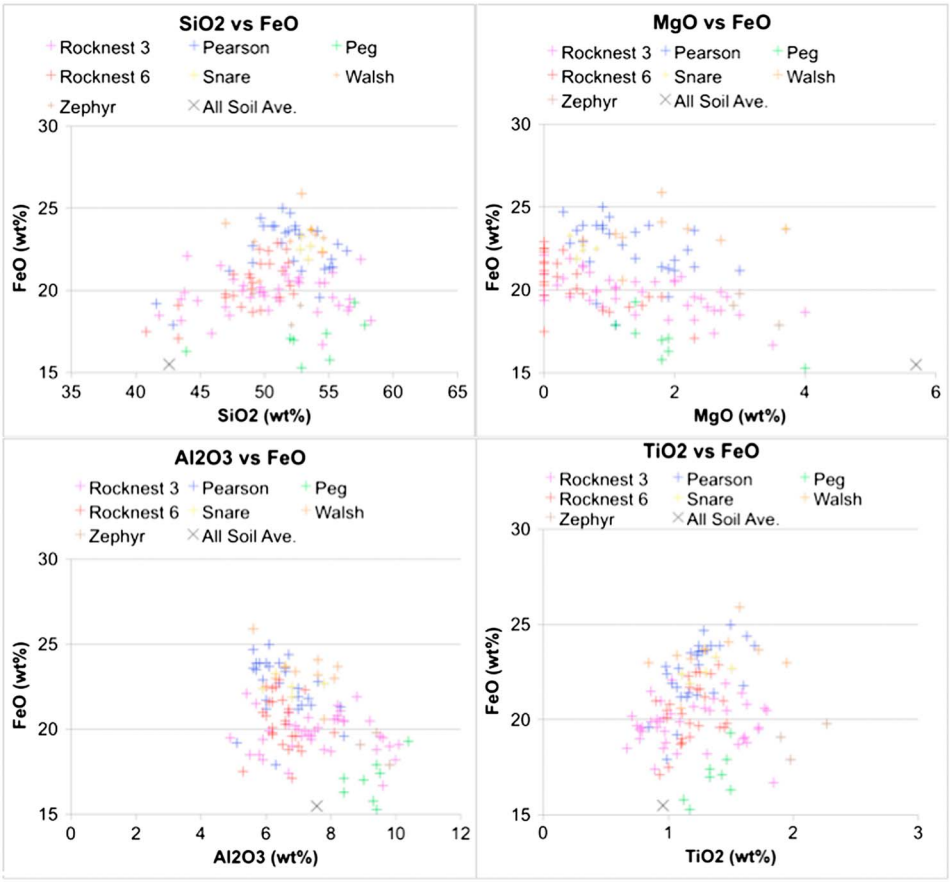

Figure 14. Elemental compositions highlighting trends with SiO_2, FeO, MgO, and TiO_2 for all of the ChemCam rock observations and for the mean ChemCam soil composition at Rocknest designated by a cross.

nominal SiO_2 abundance almost identical to that of Rocknest 3, with its relatively low FeO_T abundance [*Schmidt et al.,* 2014] and with the trends shown in Figure 13. The probable presence of a feldspar with relatively low iron may be the cause of the change in slope at higher SiO_2 abundances. The shape of the ChemCam SiO_2 versus FeO_T data distribution may also signal the presence of more than two components, such that SiO_2 abundances decrease with increasing FeO_T but also due to the presence of another nonsilicate phase. Also consistent with this, there is a slight negative trend between iron and aluminum (correlation coefficient of 0.19) (and other elements including Na and K, not shown in the figures). Magnesium and iron are not well correlated either (correlation coefficient of 0.15 for a negative iron and magnesium relationship). Interestingly, titanium appears to have the poorest correlation with FeO_T (correlation coefficient 0.010). Precision error bars for iron are ~1.8% while for titanium is 0.15%—well outside the scattered shown.

The strongest trend is the correlation between SiO_2 with total oxide weight percent of the major elements (correlation of 0.85). The all-soil average, given by an X on Figure 13, plots near the lower end of the distribution, with a total of 82 wt %. The total oxide totals exclude sulfur, phosphorus, carbon, and the halides, all of which are difficult for ChemCam to measure, along with Cr, Mn, and other minor and trace elements that are not calculated automatically as part of the PLS1 analysis. The Rocknest rock observation points range from an oxide total abundance of 74 wt % to around 100%. Rocks with lower silicate abundances have higher abundances of minerals with these elements. In Table S1, the total oxide abundances with sulfur included as sulfate approach 100%, indicating that sulfates are also present.

As with the ChemCam data, the APXS measurements show no other major element increase with the increase in iron from Rocknest 3 to Et_Then. Iron increased from 18.4 wt % to 26.4 wt % from Rocknest 3 to Et_Then; measurements for all other APXS elements were either unchanged or their abundances decreased. In particular, Ti decreased from 1.0 wt % to 0.7 wt % [*Schmidt et al.,* 2014].

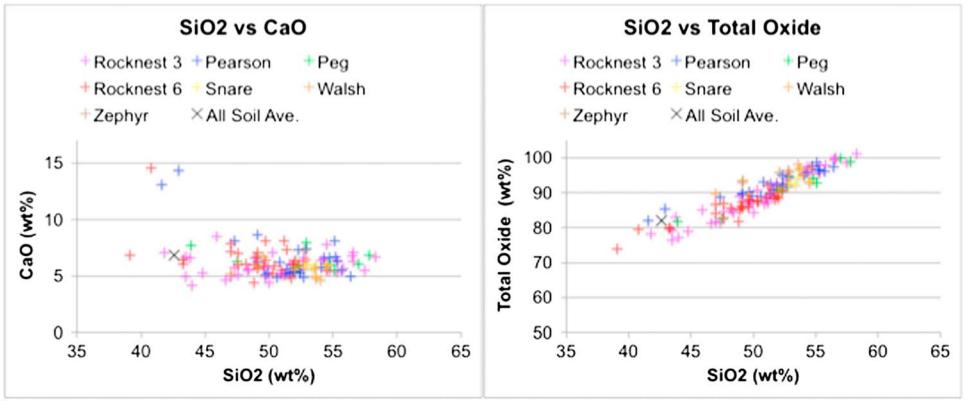

Figure 15. Elemental compositions highlighting trends with SiO_2, total oxide, and CaO for all of the ChemCam rock observations and for the mean ChemCam soil composition at Rocknest designated by a cross.

5.8. Localized Calcium Enrichments/Sulfur/Fluorine

Locations 4 and 8 on Pearson and location 12 on Rocknest 6 (Table S1 in the supporting information) display clear enrichments in CaO (up to 12.7 wt %) (Figure 15). These locations also stand out on the silica versus calcium plot in Figure 12, showing that these locations correspond to relatively low silica. Indeed, the abundances of all of the other major elements (aluminum, titanium, sodium, potassium, iron, and magnesium) also show a dip at these locations, indicating that they are not part of this high calcium phase. All three spectra show an elongated rise near 605 nm. We have tentatively identified this as a molecular line from calcium-fluoride due to a mineral such as fluoroapatite. However, a quantitative assessment of the abundances can be determined requires further laboratory work.

Figure 16 plots calcium against sulfur in moles for all of the Rocknest rock observation points. The sulfur is near the limit of quantification (shown as a vertical line on Figure 16), which is approximately the abundance of sulfur in Mars soil, 5–7 wt % SO_3. As shown in Table 4, ChemCam observations of the rocks at Rocknest (except the resistant Zephyr and Peg) show higher sulfur abundances than the nearby soils. With the exception of the outliers in Pearson and Rocknest 6 there is no general trend in the data, confirming that sulfates are likely to be intimately mixed with the matrix or widespread as microscopic veins. The two Pearson outlying points are clearly separated from the main cluster of points. These two data points lie very close to the dark blue line, representing a stoichiometric ratio for $CaSO_4$. Sulfur has a large RMSEP (4.92 wt %), and the possible presence of another high Ca-F phase (whose abundance has not been determined) could lower the amount of Ca-sulfate in these locations significantly. There is no clear H emission peak at 656 so the phase is likely anhydrous. The anomalous Rocknest 6 point can be seen lying well above the main cluster of points in Figure 16, but it is well off the 1:1 line with SO_3. Because it is not to the right of the main locus of points, we cannot say that it has any sulfur component associated with the calcium. One additional Rocknest 6 point can be seen near the top of the main cluster, and this may represent an additional point with a common enrichment of a Ca-bearing phase. In summary, the PLS summed-spectrum sulfur analysis shows that the Rocknest rocks are generally

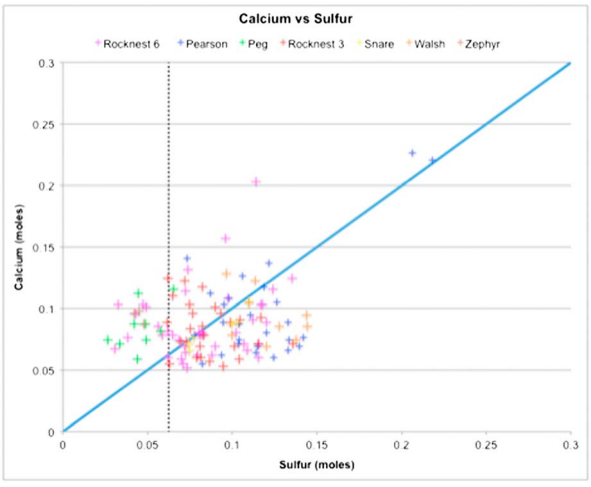

Figure 16. Ca versus S in molar fraction for all of the ChemCam rock observations in Rocknest. The diagonal line indicates stoichiometric equivalence between the two elements, as expected for Ca-sulfates. The dotted vertical line indicates the limit of quantification for sulfur from PLS 1 analysis.

Figure 17. Rocknest iron shot-by-shot analysis for representative high iron observations.

enriched in sulfur when compared to the local soil and that sulfur is distributed in the rocks. However, the identification of Ca-sulfate as the dominant sulfate is dependent on two measurements that also have evidence for another high Ca phase that has not been quantified.

5.9. Depth Profiles

ChemCam data can be analyzed on a shot by shot basis to look for compositional gradients caused by coatings and rinds. Shot-by-shot analysis of the ChemCam data shows similar patterns. The first one to five shots show compositions that are representative of a mixture of Martian dust/soils adhering to the rocks and the underlying substrate chemistry. After about five shots, compositions generally hit a plateau representative of the composition at that location. These first five shots are excluded from location measurements. Previous analysis of the interiors and exterior compositions of the Rocknest rocks showed no evidence for widespread coatings in the major elements [*Blaney et al*., 2013; *Lanza et al*., 2013]. Focusing on the iron observations, no systematic trends were observed indicating that the iron oxide is present as a coating on these rocks. Figure 16 shows example shot-to-shot elemental profiles of several high iron locations. After the surface dust is removed, the compositions are steady with depth indicating that no coatings were detected (Figure 17).

Mastcam and RMI images do not show any systematic albedo/color variations that might be due to a patchy high iron oxide coating. While albedo variations exist, they are tied to dust cover (low iron), not to high iron coatings.

6. Discussion

Textural evidence points to a soft, weakly cemented sediment with possible early diagenetic features such as the tapered cracks. The two textures (laminated/massive) have similar chemistry so differences in texture are primarily related to the depositional environment. Additionally, the presence of clearly sedimentary facies in close stratigraphic association (e.g., conglomerates, sandstones, and mudstones) [*Grotzinger et al*., 2013; *Williams et al*., 2013] creates a broader context in which to include Rocknest. No diagnostic igneous textures are observed in these rocks.

The highly variable iron content ranging from FeO_T seen by both APXS [*Schmidt et al.,* 2014] and ChemCam (ranging from ~15 to 26%) is not positively correlated with any other element which also makes it unlikely that these rocks could be a primary igneous rock.

The iron/titanium ratio in particular argues against a purely igneous formation mechanism. On Earth there are some igneous rocks with high iron content, but they are relatively rare. It is postulated that a miscibility gap exists in highly evolved magmas that lead to both high silica and high iron end-members [e.g., *Jakobsen et al*., 2005]. Such magmas have been observed in the Skaergaard intrusion in Greenland. On Earth, these dense magmas would tend to sink rather than erupt, but they might be more likely to be found at the surface on Mars due to its lower gravity. However, such melts would have quite different characteristics from those observed in the Rocknest rocks. Along with the iron enrichment one would expect high CaO/Al_2O_3, along with enrichment of P, Ti, and rare-earth elements [*Jakobsen et al*., 2005]. The Rocknest rocks do not display any of these characteristics, and in particular, the Ti abundance is relatively low and is shown not to correlate with the iron in these rocks. *Balta and McSween* [2013] recently proposed that Et_Then had a different magmatic history than Rocknest 3. They proposed that both rocks could be produced through different magmatic pathways on Mars. However, the igneous interpretation becomes problematic once the ChemCam data show the high iron in multiple locations in the same rock.

Schmidt et al. [2014] suggested that the high iron of Et_Then was related to an iron oxide cement or coating and that the overall Rocknest 3 was a volcanic or relatively immature volcanic clastic sediment. Depth profile and spatial variability of iron within the Rocknest rocks show that the iron is widely disseminated in the rock arguing against a coating for the excess iron.

Interpreting Rocknest as a sedimentary rock, the chemical variations observed are the result of sampling different abundances of grains and cement in the LIBS spot locations. The widespread distribution of highly variable iron in all the rocks plus its lack of correlation with other major elements lead us to favor iron-rich cement as an important agent of lithification in these rocks. This is consistent with *Grotzinger et al*. [2013] and *McLennan et al*. [2013] who also interpreted Rocknest 3 as a fine-grained sedimentary rock composed of basaltic detritus.

The variability of the iron oxide, the high CaO values for Rocknest, indications of sulfur, and the SiO_2/total oxide relationship suggest that nonsilicate phases played a major role in these rocks' origin. We suggest that these rocks are primary sediments that have undergone chemical alteration from their igneous precursor either during deposition and/or diagenesis including the incorporation of iron oxide cements, widely disseminated sulfates, and the depletion of Mg from the parent rock.

Passive ChemCam spectroscopy of these rocks does not show a hematite signature but a nanophase iron oxide signature [*Johnson et al*., 2013]. This suggests that the iron cement is not well crystalline and may be a number of iron oxide/oxihydroxide phases such as magnetite, nanophase hematite, and ferrihydrite. However, with no diagnostic spectral features and no CheMin measurements of mineralogy of the iron, oxide phase cannot be determined.

The presence of iron-rich fluids on Mars and in Gale is not unexpected and is supported by the detection of magnetite, likely of authigenic origin [*Vaniman et al*., 2013] in the stratigraphically subjacent Sheepbed member. Additionally, *Bridges et al.* [2013] show with thermochemical modeling that low temperature alteration 10–50°C of Gale Crater basaltic compositions (Portage soil, Ekwir_brushed) with an initially dilute brine could lead to the precipitation of Fe oxides/hydroxides and a mixture of Fe-smectite, chlorite in the Sheepbed member, similar to the mineral assemblages identified by Chemin [*Vaniman et al*., 2013].

Fraeman et al. [2013] have also identified a hematite ridge inside Gale Crater that may also have iron cements present. They interpreted the chemical signature as due to either Fe^{2+} groundwater precipitating hematite (or other iron oxide phase) or by in-place weathering. If the hematite ridge formed by groundwater precipitation, it is possible that similar iron-rich groundwater also came to the surface farther from Mount Sharp, for example, in the area of Rocknest.

Soluble calcium sulfates (and calcium-fluorine) are also present and concentrated in specific locations suggesting an additional phase of fluid interaction with the rocks. This may be related to a second round of fluids that formed the sulfate veins in the Yellowknife Bay formation [*Vaniman et al*., 2013; *McLennan et al*., 2013]. All locations seem to have some sulfate in them indicating that there is also well-distributed sulfate in these rocks—either as part of the matrix or in veins below the ChemCam RMI spatial resolution. Total oxide abundances approach 100% when sulfur is included in the values (Table 4). It is uncertain if these sulfates originated with the rocks when formed or are from a later stage alteration associated with the mobile high calcium phases seen in Sheepbed.

Given the low level of alteration seen in other nearby locations, we can explore the model that these are some kind of basaltic sandstone/siltstone cemented with iron oxides and evaluate the source of the grains. Using the ChemCam data for major rock types seen in Gale, if there were no chemical alteration in the Rocknest deposit, the sediment source for the Rocknest rocks does not appear to be the same as for other sedimentary rocks in the region (Figure 10). The low MgO in Rocknest rocks is in striking contrast to that in the lower units of Yellowknife Bay encountered just after Rocknest, which have MgO in the range of 7–9 wt % [*McLennan et al*., 2013], more normal for Martian basalts and soil. Likewise, the ChemCam observations of Bathurst Inlet yielded an average MgO of 7.6 wt %, clustering in a tight range. On the other hand, magnesium in the rocks and pebbles of Bradbury Rise is also low, measuring 3.6–4.6 wt % MgO in Jake_M [*Stolper et al*., 2013] and an average of all ChemCam measurements across Bradbury Rise over the first 48 sols gives 3.0 wt %. However, these rocks in general have higher Al_2O_3 content, at 10.7 wt % for all sol 0–48 Bradburry rocks and 9.3 wt % for Jake. Thus, either the rocks at Rocknest had a different source region than the other nearby sediments or there was a depletion of MgO in Rocknest either during formation or subsequent alteration/diagenesis.

The chemical uniqueness of the Rocknest rocks relative to their immediate surroundings raises questions about the origin of the Rocknest rocks. The timing of their deposition relative to the formation of underlying Yellowknife Bay members is well established, but uncertainties exist between the age of the Rocknest outcrop and other outcrops of the Glenelg member and between the Yellowknife bay formation and the conglomerates of Bradbury Rise [*Grotzinger et al*., 2013]. The Rocknest rocks show slight indications of similar diagenetic features to the units below it in Yellowknife Bay [*Grotzinger et al*., 2013; *McLennan et al*., 2013]. These include the calcium sulfate found in Pearson, the tapered cracks seen in the laminated rocks, and the weathering-resistant feature seen on the top of Zephyr. The latter feature bears some resemblance to the Snake feature seen near John Klein, which was interpreted to be an intrusive sandstone dike [*Grotzinger et al*., 2013]. Given these features, the Rocknest rocks very likely were in place in this location prior to the onset of these diagenetic events.

A key issue for the Rocknest rocks remains the lower MgO oxide numbers compared to potential source regions of fines. Postulating the inclusion of Bradbury rise sediments helps the situation, but other more basaltic sediments (either olivine rich sands or soils) are also required. Chemical alterations either during formation or diagenesis that reduced the amount of magnesium is also required in order to source directly from local materials observed today by ChemCam and Curiosity. One possible avenue for magnesium depletion is if the hypothesized secondary mineral that caused the pits was a relatively magnesium rich phase that has either dissolved or been preferentially eroded away (e.g., a MgCl.nH$_2$O phase).

7. Conclusions

The rocks at Rocknest represent a unique chemical unit between the Bradbury rise conglomerates and the fine-grained Bathurst rocks on the one side and potentially upward in the stratigraphic column, and the Sheepbed and Gillespie Lake units, and the Shaler and Point Lake subunits below Rocknest. Their uniqueness is largely in the variability of iron ~15–25 wt % FeO_T, and low MgO $<$ ~0–3 wt % makes them unlikely to be igneous rocks. We interpret that they are relatively fine grained sediments cemented together by an iron-rich precipitate. The rocks do not show any clear correlation between surface texture, which varies quite significantly, and chemical composition except for an erosional resistant pendent in Zephyr. Some diagenetic features including the possible presence of calcium sulfate appear in common with those observed in the lower units in Yellowknife Bay, indicating that these rocks were in place before the regional diagenetic events occurred. However, they may be related to the hematite-rich ridge that is at the edge of Mount Sharp. If so, this relationship may be clarified as the rover arrives at this feature.

Acknowledgments

This work has been conducted at the Jet Propulsion Laboratory, California Institute of Technology under a contract with the National Aeronautics and Space Administration. This work was funded by NASA's Mars Exploration Program in the U.S. and by CNES in France and by the Canadian Space Agency in Canada. We acknowledge partial funding by the Deutsche Forschungsgemeinschaft (DFG grant GO 2288/1-1) for the participation of Walter Goetz. We thank two anonymous reviewers for helpful reviews. The many other people who made the MSL mission successful are gratefully thanked and acknowledged.

References

Anderson, R. B., and J. F. Bell (2010), Geologic mapping and characterization of Gale Crater and implications for its potential as a Mars Science Laboratory landing site, *Mars*, *5*, 76–128, doi:10.1555/mars.2010.0004.

Anderson, R. C., et al. (2012), Collecting samples in Gale crater, Mars: An overview of the Mars Science Laboratory sample acquisition, sample processing and handling system, *Space Sci. Rev.*, *170*, 57–75, doi:10.1007/s11214-012-9898-9.

Balta, J. B., and H. McSween (2013), Et_Them: A possible Martian magma?, Geol. Soc. of Am., Denver, Colo.

Bish, D. L., et al. (2013), X-ray diffraction results from Mars Science Laboratory: Mineralogy of rocknest at gale crater, *Science*, *341*, doi:10.1126/science.1238932.

Blake, D., et al. (2012), Characterization and calibration of the CheMin mineralogical instrument on Mars Science Laboratory, *Space Sci. Rev.*, *170*, 341–399.

Blake, D. F., et al. (2013), Curiosity at Gale Crater, Mars: Characterization and analysis of the rocknest sand shadow, *Science*, *341*, doi:10.1126/science.1239505.

Blaney, D. L., et al. (2013), Assessment of potential rock coatings at Rocknest, Gale Crater with ChemCam, paper presented at Lunar Planet. Sci. Conf. 44, Abstract #1568.

Bridges, J. C., S. P. Schwenzer, F. Westall, and M. D. Dyar (2013), Gale Crater's Bathurst Inlet and Rocknest_3 compositions, paper presented at 44th Lunar and Planetary Science Conference, Houston, Tex, 18–22 March.

Clegg, S. M., E. Sklute, M. D. Dyar, J. E. Barefield, and R. C. Wiens (2009), Multivariate analysis of remote laser-induced breakdown spectroscopy spectra using partial least squares, principal component analysis, and related techniques, *Spectrochim. Acta, Part B*, *64*, 79–88.

Clegg, S. M., et al. (2014), Expansion of the ChemCam calibration database, paper presented at 45th Lunar and Planetary Science Conference, Abstract #2378.

Cousin, A., et al. (2013), Compositions of sub-millimeter-size clasts seen by ChemCam in Martian soils at Gale: A window into the production processes of soils, Abstract #P23C-1798 presented at 2013 Fall Meeting, AGU, San Francisco, Calif.

Dyar, M. D., J. M. Tucker, S. Humphries, S. M. Clegg, R. C. Wiens, and M. D. Lane (2010), Strategies for Mars remote laser-induced breakdown spectroscopy analysis of sulfur in geological samples, *Spectrochim. Acta B*, doi:10.1016/j.sab.2010.11.016.

Edgar L. A., D. M. Rubin, J. P. Grotzinger, J. F. Bell III, F. J. Calef III (2013), Sedimentary facies and bedform analysis observed from the Rocknest Outcrop (Sols59–100), GaleCrater, Mars, paper presented at 44th Lunar and Planetary Science Conference.

Edgett, K. S., et al. (2012), Curiosity's Mars Hand Lens Imager (MaHLI) investigation, *Space Sci. Rev.*, *170*, 259–317.

Fabre, C., S. Maurice, A. Cousin, R. C. Wiens, O. Forni, V. Sautter, and D. Guillaume (2011), Onboard calibration igneous targets for the Mars Science Laboratory Curiosity rover and the Chemistry Camera laser induced breakdown spectroscopy instrument, *Spectrochim. Acta, Part B*, *66*, 280–289.

Fraeman, A. A., et al. (2013), A hematite-bearing layer in Gale Cater Mars: Mapping and implications for past aqueous conditions, *Geology*, *41*(10), 1103–1106, doi:10.1130/G34613.1.

Gellert, R., et al. (2013), Initial MSL APXS activities and observations at Gale Crater, Mars, Lunar Planet. Sci. XLIV, 1432.

Goetz, W., et al. (2013), Morphological and chemical characteristics of sediment in Rocknest eolian sand shadow, Gale Crater, Mars, paper presented at 44th Lunar and Planetary Science Conference Abstract #1222.

Grotzinger, J. P., et al. (2012), Mars Science Laboratory mission and science investigation, *Space Sci. Rev.*, *170*, 5–56.

Grotzinger, J. P., et al. (2013), A habitable fluvio-lacustrine environment at Gale Crater, Mars, *Science*, *343*(6169), doi:10.1126/science.1242777.

Hobbs, S. W., D. J. Paull, and M. C. Bourke (2010), Aeolian processes and dune morphology in Gale Crater, *Icarus*, *210*, 102–115.

Jakobsen, J. K., I. V. Veksler, C. Tegner, and C. K. Brooks (2005), Immiscible iron- and silica-rich melts in basalt petrogenesis documented in the Skaergaard intrusion, *Geology*, *33*(11), 885–888, doi:10.1130/G21724.1.

Johnson, J. R., et al. (2013), ChemCam passive reflectance spectroscopy at Bradbury Landing, Mars, paper presented at Lunar Planet. Sci. XLIV, 1372.

Lanza, N., et al. (2013), Evidence for rock surface alteration with ChemCam from Curiosity's first 90 sols, paper presented at Lunar Planet. Sci. XLIV, 1723.

Le Mouélic, S., et al. (2013), Mars imaging by the ChemCam Remote Microscopic Imager (RMI) onboard Curiosity: The first three months, paper presented at 44th Lunar and Planetary Science Conference, held March 18–22, 2013 in The Woodlands, Texas. LPI Contribution No. 1719, p. 1213.

Leshin, L. A., et al. (2013), Volatile, isotope, and organic analysis of Martian fines with the Mars Curiosity rover, *Science*, *341*, doi:10.1126/science.1238937.

Mahaffy, P. R., et al. (2012), The sample analysis at Mars investigation and instrument suite, *Space Sci. Rev.*, *170*, 401–478.

Malin, M., and K. Edgett (2000), Evidence for recent groundwater seepage and surface runoff on Mars, *Science*, *288*, 2330–2335.

Maurice, S., et al. (2012a), The ChemCam instrument suite on the Mars Science Laboratory (MSL) rover: Science objectives and mast unit description, *Space Sci. Rev.*, *170*, 95–166, doi:10.1007/s11214-012-9912-2.

Maurice, S., A. Cousin, R. Wiens, O. Gasnault, L. Parès, O. Forni, P.-Y. Meslin, S. Clegg, and the ChemCam team (2012b), Laser induced breakdown spectroscopy (LIBS) spot size at stand-off distances with ChemCam, Lunar and Planetary Science Conference 43rd #2899.

McLennan, S. M., et al. (2013), Elemental geochemistry of sedimentary rocks at Yellowknife Bay, Gale Crater, Mars, *Science*, *343*(6169), doi:10.1126/science.1244734.

McSween, H. Y., G. J. Taylor Jr., and M. B. Wyatt (2009), Elemental composition of the Martian crust, *Science*, *324*, 736–739.

Meslin, P. Y., et al. (2013), Soil diversity and hydration as observed by ChemCam at Gale Crater, Mars, *Science*, *341*, doi:10.1126/science.1238937.

Milliken, R. E., J. P. Grotzinger, and B. J. Thomson (2010), Paleoclimate of Mars as captured by the stratigraphic record in Gale Crater, *Geophys. Res. Lett.*, *37*, 1–6, doi:10.1029/2009GL041870.

Minitti, M. E., et al. (2013), MAHLI at the Rocknest sand shadow: Science and science-enabling activities, *J. Geophys. Res. Planets*, *118*, 2338–2360, doi:10.1002/2013JE004426.

Sallé, B., J.-L. Lacour, E. Vors, P. Fichet, S. Maurice, D. A. Cremers, and R. C. Wiens (2004), Laser-induced breakdown spectroscopy for Mars surface analysis: Capabilities at stand-off distance and detection of chlorine and sulfur elements, *Spectrochim. Acta B*, *59*, 1413–1422.

Sautter, V., et al. (2014), Igneous mineralogy at Bradbury Rise: The first ChemCam campaign at Gale Crater, *J. Geophys. Res. Planets*, *119*, 30–46, doi:10.1002/2013JE004472.

Schmidt, M. E., et al. (2014), Geochemical diversity in first rocks examined by the Curiosity Rover in Gale Crater: Evidence for and significance of an alkali and volatile-rich igneous source, *J. Geophys. Res. Planets*, *119*, 64–81, doi:10.1002/2013JE004481.

Silvestro, S., D. A. Vaz, R. C. Ewing, A. P. Rossi, L. K. Fenton, T. I. Michaels, J. Flahaut, and P. E. Geissler (2013), Pervasive Aeolian activity along rover Curiosity's traverse in Gale Crater, Mars, *Geology*, *41*, 483–486, doi:10.1130/G34162.1.

Stack, K. M., et al. (2014), Diagenetic origin of nodules in the Sheepbed member, Yellowknife Bay formation, Gale crater, Mars, *J. Geophys. Res. Planets*, *119*, 1637–1664, doi:10.1002/2014JE004617.

Stolper, E. M., et al. (2013), The petrochemistry of Jake_M: A Martian mugearite, *Science*, *341*, doi:10.1126/science.1239463.

Sumner, D. Y., et al. (2013), Preliminary geological map of the Peace Vallis Fan integrated with in situ mosaics from the Curiosity Rover, Gale Crater, Mars, paper presented at Lunar Planetary Science Conference Abstract #1699.

Thompson, B. J., N. T. Bridges, R. Miliken, A. Baldridge, S. J. Hook, J. K. Crowley, G. M. Marion, C. R. De Souza, A. J. Brwon, and C. W. Weitz (2011), Constraints on the origin and evolution of the layered mound in Gale Crater, Mars using Mars Reconnaissance Orbiter data, *Icarus*, *214*, 413–432, doi:10.1016/j.icarus.2011.05.002.

Tucker J. M., M. D. Dyar, M. W. Schaefer, S. M. Clegg, and R. C. Wiens (2010), Optimization of laser-induced breakdown spectroscopy for rapid geochemical analysis, *Chem. Geol.*, *277*, 137–148, doi:10.1016/j.chemgeo.2010.07.016.

Vaniman, D., M. D. Dyar, R. Wiens, A. Ollila, N. Lanza, J. Lasue, J. M. Rhodes, S. Clegg, and H. Newsom (2012), Ceramic ChemCam Calibration Targets on Mars Science Laboratory, *Space Sci. Rev.*, *170*, pp. 229–255, doi:10.1007/s11214-012-9886-0.

Vaniman, D., et al. (2013), Mineralogy of a mudstone on Mars, *Science*, *343*(6169), doi:10.1126/science.1243480.

Wiens, R. C., et al. (2012), The ChemCam instruments on the Mars Science Laboratory (MSL) rover: Body unit and combined system performance, *Space Sci. Rev.*, *170*, 167–227, doi:10.1007/S11214-012-9902-4.

Wiens, R. C., et al. (2013a), Pre-flight calibration and initial data processing for the ChemCam laser-induced breakdown spectroscopy instrument on the Mars Science Laboratory rover, *Spectrochim. Acta, Part B*, *82*, 1–27, doi:10.1016/j.sab.2013.02.003.

Wiens, R. C., et al. (2013b), Compositions determined by ChemCam along Curiosity's traverse from Bradbury Station to Glenelg in Gale Crater, Mars, Lunar Planet. Sci. LXIV, 1363.

Williams, R. M. E., et al. (2013), Martian fluvial conglomerates at Gale Crater, *Science*, *340*, 1068–1072.

Wray, J. J. (2013), Gale Crater: The Mars Science Laboratory/Curiosity rover landing site, *Int. J. Astrobiol.*, *12*(1), 25–38, doi:10.1017/S1473550412000328.

Yingst, R. A., et al. (2013), Characteristics of pebble- and cobble-sized clasts along the Curiosity rover traverse from Bradbury Landing to Rocknest, *J. Geophys. Res. Planets*, *118*, 2361–2380, doi:10.1002/2013JE004435.